Copyright

by

Vijay Anirudh Premnath

2023

The Thesis Committee for Vijay Anirudh Premnath
Certifies that this is the approved version of the following Thesis:

Fabrication and Process Optimization for Functional 3D Periodic Nanolattices

APPROVED BY
SUPERVISING COMMITTEE:

Chih-Hao Chang, Supervisor

Micheal Cullinan

Fabrication and Process Optimization for Functional 3D Periodic Nanolattices

by

Vijay Anirudh Premnath

Thesis

Presented to the Faculty of the Graduate School of

The University of Texas at Austin

in Partial Fulfillment

of the Requirements

for the Degree of

Master of Science in Engineering

The University of Texas at Austin

December 2023

Acknowledgements

I would like to express my deepest gratitude to Dr. Chih-Hao Chang, whose expertise, understanding, and patience added considerably to my graduate experience. His willingness to give his time so generously has been very much appreciated. I am truly thankful for the guidance, insightful critiques, and the encouragement I received. I extend my thanks to the members of my advisory committee, Dr. Micheal Cullinan, for their invaluable feedback that inspired further insights into my research.

My sincere appreciation also goes to the faculty and staff in the Mechanical Engineering Department at The University of Texas at Austin, whose knowledge and technical assistance were always available when I needed it. I am particularly grateful for the assistance given by the Teaching Assistants as well as fellow Research Assistants. I also acknowledge my colleagues from the Nanostructures and Nanomanufacturing Lab, whose camaraderie, support, and exchange of ideas were immensely beneficial throughout my studies. I must also express my gratitude to my friends and family for all their encouragement, understanding, and love.

This work was performed at UT Austin Texas Materials Institute (TMI), the Nanomanufacturing System for mobile Computing and Energy Technologies (NASCENT), and Texas Nanofabrication Facilities, which is supported by the National Science Foundation (NSF) as part of the National Nanotechnology Coordinated Infrastructure (NNCI) grant NNCI-2025227. This work was funded by the Energy Institute at the University of Texas at Austin.

Abstract

Fabrication and Process Optimization for Functional 3D Periodic Nanolattices

Vijay Anirudh Premnath, M.S.E,
The University of Texas at Austin, 2023

Supervisor: Chih-Hao Chang

This research focuses on the development and analysis of advanced nanolattices and three-dimensional (3D) nanostructures, showing their significance in nanophotonics, integrated circuits, lasers, optical systems, and various other applications. Nanolattices are characterized by their periodic lattice arrangement, hollow-core, and thin-shell elements, are fabricated using thin-film deposition on 3D polymer templates. These structures offer immense potential in mechanical, optical, and thermal applications, due to their unique properties. However, a major challenge in their fabrication is the residual polymer left within the nanolattice, which can impede their performance. To address this, the study investigates three different polymer template removal techniques, including oxygen plasma etching, solvent dissolution, and thermal desorption, to determine their effectiveness in eliminating residual polymer. The removal rates and effectiveness of each method are quantitatively analyzed using spectroscopic ellipsometry, a technique that precisely measures the effective refractive index and calculates the amount of residual polymer. The findings reveal that thermal treatment is the most effective in template removal, providing

a path to enhance nanolattice fabrication for various applications. Additionally, the research utilizes a three-phase Maxwell–Garnett effective medium model to estimate the residual polymer in nanolattices.

Parallelly, the research delves into the fabrication of 3D nanostructures, specifically opal structures, which are spatially aligned to an array of holes defined in the photoresist. This approach employs colloidal lithography to pattern a hexagonal array of holes, guiding the assembly of colloidal particles into 3D opal structures. This method ensures the alignment of the 3D opal structures with the 2D hole array, enhancing spatial-phase coherence and minimizing defects. The polymer patterns serve as a sacrificial template for atomic layer deposition, enabling the creation of free-standing nanolattices. These nanolattices are subsequently coated with a thick layer of titanium oxide, demonstrating their mechanical stability. The resulting structures boast high porosity, essential for creating low-index materials in nanophotonics. Additionally, the study incorporates nature-inspired nanostructures, employing biomimetic principles to enhance the functionality and efficiency of these materials. These nature-inspired designs, mimicking the structures found in natural organisms, provide solutions for light manipulation and structural resilience. These nanostructures, with controlled height and precise deposition, are ideal for applications in Bragg reflectors, nanophotonics, and optical multilayers, marking a significant advancement in the field of nanostructured materials. The study's findings on template removal, 3D nanostructure fabrication, and biomimetic design open new avenues for research and development in this rapidly evolving field, promising enhancements in the efficiency and functionality of nanostructured materials and devices.

Table of Contents

List of Tables 9

List of Figures 10

CHAPTER 1: INTRODUCTION 13

1.1 *Bio Inspired 3D Nanolattices*..13

1.1.1. Properties of Nanostructures: -- 13

1.1.2. Engineered Nanostructures:-- 15

1.1.3. Nanostructures in Nature: -- 17

1.2 *Fabrication of 3D Nanostructures*--- 19

1.3 *Goal of the thesis* -- 24

CHAPTER 2: INVESTIGATION OF POLYMER TEMPLATE REMOVAL TECHNIQUES IN THREE-DIMENSIONAL THIN-SHELL NANOLATTICES ---------------------------------- 26

2.1 *Introduction* --- 26

2.2 *Experimental Methodology* --- 27

2.2.1. Fabrication procedures:--- 27

2.2.2. Fabrication Result: -- 29

2.2.3.Optical Characterization:-- 33

2.3 *Results and Discussion* -- 34

2.3.1. Spectroscopic Ellipsometry measurements: ------------------------------------ 34

2.3.2. Characterization of Residual Resist:-- 35

2.3.3 Theoretical validation of Residual Resist: --------------------------------------38

2.4 *Conclusion* ---------- 41

CHAPTER 3: FABRICATION OF THREE-DIMENSIONAL OPAL NANOLATTICES USING TEMPLATE-DIRECTED COLLOIDAL ASSEMBLY ---------- **43**

3.1 *Introduction* ---------- 43

3.2 *Fabrication Procedure* ---------- 44

3.3 *Results and Discussion* ---------- 47

3.3.1. Patterning of resist using UV Lithography: ---------- 47

3.3.2. Formation of Multilayer Inverse Opal structures: ---------- 50

3.3.3. Fabrication issues: ---------- 54

3.4 *Conclusion* ---------- 57

CHAPTER 4: CONCLUSION AND FUTURE WORK ---------- **59**

REFERENCES ---------- 61

List of Tables

Table 1: Table 1 – Variation of indices and MSE values of lattices with increase in time of exposure for 0, 5, 10 and 15 minutes, when subjected to NMP solvent---37

Table 2: Table 2 – Variation of indices and MSE values of lattices with increase in time of exposure for 0, 5, 10 and 15 minutes, when subjected to O2PE process --38

List of Figures

Figure 1 – Different types of photonic crystals depending on the direction in which the dielectric profiles are infused. (a) 1D (b) 2D and (c) 3D photonic crystals ----------------- 16

Figure 2 – (a) Periodic anti-reflection lattices inspired from Moth eye structures (b) Tunable lattices inspired from Neon tetra, which is magnetically tuned------------------------------ 18

Figure 3 – Schematic of the nanolattice fabrication process involving (a) deposition of ARC, PR, and nanospheres with 500 nm diameter followed by lithography and development. (b) Samples are subjected to ALD over the template. (c) Three types of resist removal techniques include (i) thermal desorption, (ii) solvent dissolution, and (iii) oxygen plasma etching. (d) Final thin-shell lattice after polymer is removed--------------------------------- 27

Figure 4 – Fabrication results of nanolattices after removing the polymer template in the furnace (thermal desorption). The SEM image of nanolattices fabricated with 500 nm diameter particles and 300 nm resist height--- 30

Figure 5 – Images of lattice post subjecting them to resist removal processes. (a) and (b) SEM images with prominent gray regions representing 5 min of NMP exposure, (c) and (d) images depict faint grey regions for resist removal in the nanolattices after 10 min of NMP dissolution, (e) SEM image with prominent gray regions representing 5 min of plasma etching, (f) SEM image depict milder gray regions for resist removal in the nanolattices after 10 min of the plasma etching process--- 32

Figure 6 – Measured and fitted Δ/Ψ values over the wavelength spectrum for a nanolattice sample subjected to thermal desorption. The close agreement between the two indicates that the measured effective index is accurate-- 34

Figure 7 – (a) Measured effective refractive indices of the nanolattice vs process time. (b) Calculated volume fraction of residual polymer vs process time using the MG model---- 41

Figure 8 – Fabrication process for hollow opal nanolattice. a) deposition of ARC and PR layers on silicon substrate over which the nanospheres are transferred manually. b) Exposure and development of photoresist. c) Assemble additional PS nanospheres on the photoresist template. d) Deposit conformal ALD coating on polymer nanostructures. e) Planarization coating of PR and deposit TiO_2. f) Removal of PR and buffer layer by temperature treatment-- 47

Figure 9 – Cross-sectional SEM images of fabricated photoresist template. a) Top view of patterned photoresist after exposure and development. b) Side view of patterned resist exposed from the uniform hexagonal closed packing of nanospheres----------------------- 49

Figure 10 – Illustration of proposed high porosity opal nanostructure with capping film to create a high index mismatch interface. The schematic a) depicts a stack of desired nanostructure consisting of silicon substrate, porous Al_2O_3 nanostructures, hollow opal nanostructures, and a solid TiO_2 layer. b) represents the SEM image of the fabricated sample depicting the stacking of nanostructure-- 51

Figure 11 – SEM images of fabricated opal nanostructures containing a) single, b) two, c) three, and d) four nanosphere assembly layers prior to deposition of ALD film----------- 54

Figure 12 – SEM images of fabricated structures consisting of macro and microcracks with a) low magnification of 100 µm scale bar and b) higher magnification of 20 µm scale bar. c) Primary micro crack formation over titanium oxide layer and d) branched microcracks from the primary microcracks which have thickness in the order of 300 nm.--------------55

Figure 13 – SEM images of patterned structures showing the (a) presence of dust particles on the structures, resulting in disrupted HCP formation in the neighboring zones, and (b) particle arrangement defects that arise from inherent shape and size defects in individual spherical nanospheres-- 57

CHAPTER 1: INTRODUCTION

1.1 *Bio-Inspired Nanostructures*

1.1.1. PROPERTIES OF NANOSTRUCTURES:

Nanoscience and nanotechnology span a vast range of research and applications, making significant impacts in various fields due to the scaling laws compared to bulk materials **[1-13].** The dimensions of these materials largely influence their characteristics and utility. 0-dimensional (0D) nanostructures, such as quantum dots, exhibit quantum confinement in all three spatial dimensions, leading to unique electronic and optical properties that are utilized in applications like biomedical imaging and photovoltaics. 1-dimensional (1D) nanostructures, including nanowires and nanotubes, are characterized by confinement in two dimensions. Such materials have high aspect ratios, which are beneficial for their electrical conductivity and mechanical strength and making them ideal for use in nanoelectronics and as reinforcing agents in composite materials. 2-dimensional (2D) nanostructures such as graphene and transition metal dichalcogenides, consisting of single layers of atoms, exhibit extraordinary electrical, thermal, and mechanical properties due to their two-dimensional confinement, finding roles in applications from sensors to energy storage devices.

Three-dimensional (3D) nanostructures, distinguished by their unique properties, due to the improved scaling of physical properties to the nanoscale **[10, 11, 37].** For example, in these nanolattice structures the surface area-to-mass ratio increases dramatically. This increase is due to the mass varying in proportion to the cube of the diameter, while the surface area is proportional to the square. Such geometric scaling

elevates the surface-to-mass ratio of nanoparticles substantially when compared to their larger, macro-scale equivalents. This elevated ratio significantly enhances the role of surface energy over the inertial forces that are more dominant in larger-sized objects. Consequently, nanoparticles are highly efficient in forming complex, self-organizing structures due to the surface effects being dominant.

Additionally, porous 3D nanostructures, known for their high surface-to-volume ratios, represent a significant leap in energy storage technology. These materials, including those formed using opal templates or nanorod assemblies, provide increased efficiency in energy storage systems **[9].** Their porous nature allows for rapid ion transport, facilitating a larger interface for electrochemical reactions and boosting the performance of devices like batteries in terms of efficiency, speed, and capacity **[9].** Beyond energy storage, 3D nanostructures exhibit a plethora of unique mechanical, optical, and chemical properties. For instance, their mechanical strength and lightweight nature make them ideal for use in aerospace composites, protective coatings, and nanoelectromechanical systems **[3-6,30].** Optically, these materials exhibit novel behaviors due to their ability to manipulate light at the nanoscale, leading to applications in photonic devices and novel display technologies.

Chemically, 3D nanostructures offer remarkable catalytic properties, with their high surface area enabling more active sites for chemical reactions. This characteristic is crucial in applications like environmental remediation and chemical synthesis. Additionally, their enhanced reactivity and selectivity opens new avenues in nano catalysis and sensor technology. The thermal properties of 3D nanostructures are equally noteworthy. Their enhanced thermal conductivity and stability are vital in electronics cooling, thermoelectric materials, and heat management systems in various engineering applications. The interplay

of these properties at the nanoscale makes 3D nanostructures a cornerstone in the development of advanced materials, driving innovation across a spectrum of scientific and engineering disciplines **[6-8].** The precise engineering and utilization of these properties herald an era where the manipulation and application of materials at the nanoscale will be central to technological advancements.

1.1.2. ENGINEERED NANOSTRUCTURES:

Engineered 3D nanostructures exhibit distinctly unique optical interactions, diverging significantly from those observed in bulk materials, primarily due to their nanoscale dimensions. When light interacts with nanostructured materials of dimensions comparable to its wavelength, the interaction dynamics are altered. This scale of structure can lead to optical phenomena, such as photonic bandgap formation, that are not present in larger-scale materials. In the context of 3D photonic crystals (dielectric profiles infused along three dimensions to enable light manipulation), as shown in Figure 1, the variation in dielectric properties on the scale of the wavelength of light can lead to the generation of a photonic bandgap **[10,11].** This bandgap occurs due to the periodic modulation of the refractive index at the nanoscale, which manipulates the propagation of light through the material for different modes **[12].** When light of specific wavelengths encounters these periodic structures, it can result in complete reflectance at those wavelengths, effectively creating a bandgap similar to the electronic bandgap in semiconductors. This phenomenon is critical in the design and function of photonic crystals and low index materials **[13-16],** which can be engineered to reflect specific wavelengths almost entirely, thereby controlling the flow of light in an accurate manner. A 1D PhC often acts as an effective Bragg reflector reaching 100% reflectance values for broad range of wavelengths **[12].**

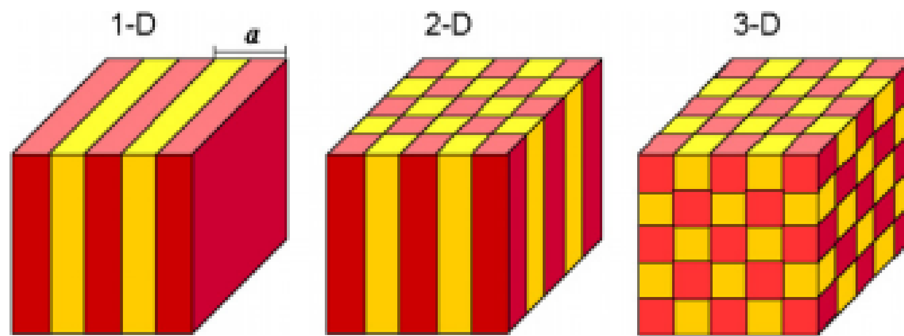

Figure 1 – Different types of photonic crystals depending on the direction in which the dielectric profiles are infused. (a) 1D (b) 2D and (c) 3D photonic crystals. **[14]**

The unique ability of 3D photonic crystals to manipulate light makes them highly suitable for a range of optical applications. They can be utilized in the creation of waveguides, where the controlled direction and confinement of light are essential. The precise engineering of the bandgaps in these structures allows for the efficient transmission of light within certain wavelength ranges while blocking others, making them ideal for integrating into photonic circuits as filters or reflectors.

Moreover, the incorporation of 3D nanostructures in optical components can enhance the performance of various optical devices. By tailoring their structural properties, these nanostructures can be used to develop prisms, lenses, and other components with improved efficiency, miniaturization, and novel functionalities. These enhancements are particularly important in the fields of imaging, laser technology, and integrated photonics, where controlling light at such a fine scale opens new possibilities for device performance and application. Furthermore, 3D nanostructures can play a vital role in the development of next-generation display technologies, sensors, and energy-efficient lighting systems. The ability to engineer materials at this level allows for the manipulation of light-matter

interactions in ways that were previously difficult to achieve, leading to highly efficient light emission, capturing, and conversion processes. This precision control over optical properties is not only pivotal for current technologies but also paves the way for the emergence of new quantum and nano-optoelectronic devices, harnessing the uniqueness of quantum mechanics and nanoscale physics to explore beyond the current limitations of optical technology.

1.1.3. NANOSTRUCTURES IN NATURE:

Nanotechnology and biomimetic materials frequently incorporate ideas from the natural world, with the help of advanced analytical techniques that explore the natural structures. Among these, Figure 2 displays some examples. Specifically, Figure 2(a) focuses on nanostructures designed after the anti-reflective characteristics of moth eyes **[19,20].** The eyes of a moth are covered with minute, conical pillars that effectively reduce light reflection by gradually altering the refractive index from air to the eye surface. This design minimizes glare, aiding the moth's nocturnal vision. Drawing inspiration from this, similar antireflection nanostructures have been fabricated to lower reflectivity and increase the transmission of light, proving useful in enhancing the efficiency of solar panels and electronic displays.

Figure 2(b), on the other hand, shows innovations inspired by the color-shifting skin of neon tetras **[21].** These fish change color through the interaction of light with microscopic structures in their skin, which reflect light in different ways. The vivid, dynamic colors of neon tetra fish are a result of the microscopic structure of their scales. These scales contain layers of crystalline cells that interfere with incoming light, selectively reflecting specific

wavelengths that result in the fish's perceived color. By altering the orientation or spacing of these layers, the fish can effectively change its color. This phenomenon, known as structural coloration, provides an excellent blueprint for developing materials that can manipulate light in complex ways. This biological trick has influenced the design of dynamic color-changing systems in ferrofluids. By applying magnetic fields, the fluid's particles align in various formations, mirroring the light-manipulating action seen in neon tetras. Such technology has potential applications in displays, security printing, and sensing devices, showcasing how the complexity of nature can be harnessed in practical, technological solutions.

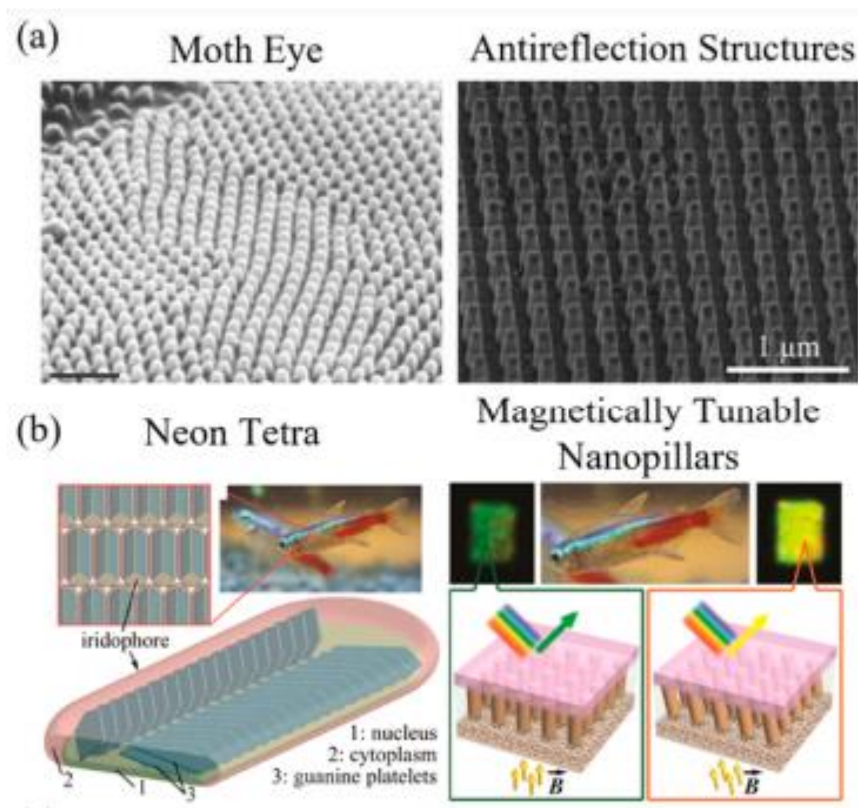

Figure 2 – (a) Periodic anti-reflection lattices **[19]** inspired from Moth eye structures **[18]** (b) Tunable lattices inspired from Neon tetra **[21],** which is magnetically tuned.

The strategy of utilizing porosity to engineer materials with lower density and weight, while maintaining structural integrity, is a principle mimicking nature and valuable in the field of optics. This principle, particularly when applied to the design of nanostructures, involves introducing tiny voids or air gaps into the material at a nanoscale level. Doing so effectively lowers the material's overall refractive index — a measure of how much light bends or refracts as it enters the material. In the context of optical materials, a lower refractive index is highly desirable to increase index mismatch. It minimizes the amount of light that is reflected off the surface of the material, thereby maximizing the amount of light that is transmitted or absorbed. This concept is critical in the development of anti-reflective coatings and materials, similar to those found in the natural world — such as in the structure of a moth's eye. Moth eyes structures create a gradual variation in the refractive index from the air (index of 1) to the solid eye surface, effectively manipulating the light and reducing reflection, and allowing the moth to see better at night without the interference of reflections. Incorporating these bioinspired design principles into the fabrication of 3D nanostructures enables the development of optical devices. For instance, in photovoltaic cells, materials with a lower refractive index and anti-reflective properties can absorb more sunlight, translating to higher energy conversion efficiency. In optical sensors, materials that mimic the dynamic color changes of the neon tetra can be used to create sensors that change color in response to chemical, biological, or mechanical stimuli.

1.2 *Fabrication of 3D Nanostructures*

While 3D nanostructures have significant mechanical, thermal, electrical, and optical applications, the manufacturing of such materials at a large scale is still a significant challenge **[41].** Existing nanofabrication processes can be grouped into two categories: Top-

down and bottom-up techniques. Top-down techniques generally involve lithography to define the pattern and material deposition or removal from the bulk to achieve nanoscale feature sizes. The bottom-up techniques focus on assembling the nanoscale elements into functional components using interactions between the elements. This process is complicated and has lower throughput compared to top-down techniques. Bottom-up not only involves the arrangement of elements (such as atoms, particles, DNA, and proteins) into desirable structures but also in the formation of unprompted assembly units into organized structures in the most energy-stable configurations **[22].** For instance, the formation of hexagonal closed packed structures by nanosphere arrays in a monolayer is owed to the least surface energy configuration of spheres.

The development of nanostructures with a high refractive index mismatch and porous nanolattices utilizes fabrication techniques to overcome the limitations of traditional bulk materials. Traditional materials like calcium fluoride, with its relatively low refractive index of 1.39 **[17],** can no longer meet the requirements of advanced photonic elements, which rely on a high contrast in refractive index. To address this, methods such as glancing angle deposition (GLAD) **[13, 15]** and sol-gel **[16]** processes have been employed. GLAD is a physical vapor deposition process where the substrate is positioned at an oblique angle relative to the vapor source. This setup allows for the creation of nanostructures with highly controlled, columnar shapes, and inherent porosity, leading to a reduction in the effective refractive index. The control over the angle and rotation of the substrate during deposition enables the creation of tailor-made structures with desired optical properties. The sol-gel process, on the other hand, is a chemical route to fabricate nanostructured materials. It involves the transition of a system from a liquid "sol" into a solid "gel" phase. By manipulating the precursor solutions, processing conditions, and subsequent drying and

heat-treatment steps, porous nanostructures with a range of refractive indices can be synthesized. This method is particularly useful for creating oxide-based materials with controlled porosity. These nanolattices can be crucial in developing Bragg reflectors or 1D PhCs, where the high contrast in refractive index between the layers results in perfect reflectivity across a broader wavelength range. Furthermore, by building multilayered photonic structures using these nanostructured materials, it's possible to create gradient-index profiles. These profiles allow for a spatial variation in refractive index, ideal for anti-reflective coatings and other applications where control over light propagation is paramount. By layering materials with different refractive indices, one can effectively manipulate the path of light, reducing reflection and enhancing transmission, which is important in applications ranging from efficient solar panels to stealth technology. This control and the ability to tailor the optical properties at the nanoscale mark a leap from traditional materials, paving the way for more advanced and efficient photonic devices.

Optical lithography, a popular fabrication technique in the microfabrication industry, consists of using a photosensitive polymer, typically a photoresist, is selectively exposed to light to form a latent image corresponding to the desired pattern **[27].** This process is central to various applications, ranging from semiconductor device fabrication to the creation of intricate microfluidic devices. The evolution of this technique, particularly the implementation of phase shift lithography, has expanded its capabilities, especially in the patterning of three-dimensional (3D) structures **[28-32].** The fundamental principle of phase shift lithography involves the use of a periodic phase element, similar to a traditional photomask, but with the ability to induce a phase shift in the light passing through it. This phase shift is crucial as it results in the formation of a diffraction interference pattern upon

the photoresist layer. The uniqueness of this technique is in its ability to create complex, volumetric intensity patterns that are not achievable with standard lithography. The patterns' dimensions and the angle of diffraction are controlled by the interplay between the period of the phase mask and the wavelength of the light used. An approach to phase shift lithography is the employment of self-assembled nanospheres, typically arranged in a hexagonal close-packed structure **[32,33].** This configuration, when exposed to ultraviolet (UV) illumination, leads to the emergence of a 3D intensity pattern within the photoresist **[31].** The underlying principle of this phenomenon is the Talbot effect, a near-field diffraction effect that generates self-images of a periodic structure at certain distances, known as the Talbot distances. These distances are where the intensity patterns due to the interference of light rays repeat along the axial length of the nanosphere arrays. Utilizing this method eliminates the need for conventional, physically etched masks. Instead, the pattern is generated through the natural self-assembly of colloidal particles, presenting a cost-effective and versatile alternative. The resulting 3D photoresist structures can subsequently act as sacrificial templates for further processes.

Atomic Layer Deposition (ALD) is a thin film deposition method distinguished by its capability to precisely control film thickness down to the atomic scale, which is highly beneficial in the manufacture of nanostructures and devices with requirements for thin film uniformity and conformity **[34,35].** Unlike other film deposition techniques, ALD operates in a cyclic manner, involving sequential, self-limiting reactions. Each ALD cycle includes four primary steps: precursor adsorption, precursor reaction (and purging), reactant adsorption, and reactant reaction (followed by a purge). The precision of ALD comes from the chemical reactions occurring at the substrate's surface, where precursor molecules chemically bond until the surface-active sites are fully saturated, allowing the film to grow

by only one atomic layer per cycle. This method provides remarkable control over film thickness, crucial in many optical and electronic applications. The temperature during ALD is crucial and needs fine-tuning; it must be sufficiently high to promote chemical reactions between the precursor and the surface but low enough to prevent precursor decomposition. The main advantage of ALD is its uniformity and conformity, especially useful for coating high-aspect-ratio structures, as often required in advanced semiconductor devices, optical materials, and nanostructures. However, the technique's deposition rate is typically slower than other methods, and the choice of precursors (which must be reactive and volatile) is another challenge.

In the context of photonic devices, the accurate control ALD offers is crucial for engineering structures with specific optical properties, such as low refractive indices necessary for antireflective coatings or photonic crystals **[34-36].** As such, ALD's role in nanotechnology is crucial, driving the development of materials and devices with high precision and capabilities, vital for the continuous improvement of nanoscale fabrication. Recent advancements in nanolattice fabrication using ALD have reported the achievement of materials with refractive indices as low as 1.025 **[34].** This reduction in refractive index is not only pivotal in enhancing the performance of photonic devices but also opens new avenues in areas like sensor technology and biomimicry. However, there are challenges to this approach. For instance, the maximum height of the resultant low-index structures is currently constrained by the thickness of the photoresist used. Additionally, the optical absorption characteristics of the photoresist itself can limit the effective depth of pattern formation. Overcoming these limitations requires innovative approaches in photoresist formulation and curing processes to enhance both the depth of penetration of the light and the subsequent pattern resolution.

Furthermore, the integration of such low-index nanostructures with solid, high-index layers presents another significant challenge, particularly in the fabrication of photonic multilayers. The interface between these different materials needs to be precisely managed to maintain optical quality and ensure effective light propagation. This is crucial in applications such as antireflective coatings, where a gradient in refractive index is desirable. Thus, phase shift lithography, especially when combined with techniques like ALD, presents a highly promising avenue for the fabrication of nanostructured materials with tailored optical properties. The innovation in this field, driven by the desire to mimic complex natural structures and enhance the functionality of photonic devices, stands at the forefront of current scientific research. The continuous refinement of these methods, addressing the limitations and expanding the capabilities, is set to propel the development of next-generation optical materials and devices.

1.3 *Goal of the thesis*

This thesis investigates various methodologies for polymer template eradication. These included oxygen plasma etching, solvent dissolution, and thermal desorption, aiming to strip the resist. The efficiency of resist removal and time of exposure at which these processes eliminate the resist were measured using spectroscopic ellipsometry. This technique afforded us the ability to confirm the effective refractive index and calculate the remaining polymer. For a thorough understanding of the residual polymer within the nanolattices, we applied a three-phase Maxwell-Garnett effective medium theory. This allowed us to model and calculate the remaining polymer material, providing critical insight

into the efficiency of the different removal techniques and informing future directions for optimizing the fabrication process of these nano-engineered structures.

Building upon the foundational research, we present development of highly porous 3D nanolattices constructed on a lithographically fabricated array of holes, utilizing hollow-core opal structures for alignment. These intricate structures are crafted by the conformal coating of an Al_2O_3 film over a porous resist patterned by advanced phase shift lithography. This process yields a porous matrix with multiple levels of hollow opal nanolattices. The precision in the thickness of the opal nanostructures is adjustable, depending on the number of nanosphere assembly layers, with capabilities ranging from a one layer to four layers. These opal layers provide manipulation over the nanolattice's height, a crucial factor in tailoring the photonic characteristics of the structure. After a planarization phase, a TiO_2 layer is uniformly deposited, serving as a capping layer that not only seals the structure but also allows for the subsequent addition of other layers. This arrangement exploits the significant refractive index disparity between the porous Al_2O_3 nanolattice and the TiO_2 layers, promising potential uses in the fabrication of photonic crystals and waveguides.

CHAPTER 2: INVESTIGATION OF POLYMER TEMPLATE REMOVAL TECHNIQUES IN THREE-DIMENSIONAL THIN-SHELL NANOLATTICES[1]

2.1 *Introduction*

The use of sacrificial templates is a critical step in the fabrication of nanolattices and inverse opal processes. Inverse opal structures refer to closed packed arrangement of spheres, wherein the spheres are volumetrically filled with voids, but have material at their boundaries. While the template plays an important role in forming the nanolattice geometry, it needs to be fully removed to result in a highly porous nanolattice structure. Investigating different polymer removal techniques, such as N-Methyl Pyrrolidone (NMP), oxygen plasma etching, and thermal desorption process, is crucial for both scientific advancement and practical applications. This research is important in material science, especially in polymer sciences, where understanding polymer template or scaffold removal is key for a range of applications from mechanical metamaterial, photonics, and biomedicine.

Common techniques for polymer removal includes NMP solvent, oxygen plasma etching, and thermal desorption, however it is not well understood which process is the most advantageous when it comes to process efficiency in removal of resist, time, and precision control over material microstructures. This precision is essential in industries like semiconductor manufacturing and optical device production, where small details affect product performance. Additionally, controlling the physical properties such as refractive indices of lattices can lead to new developments in optics and photonics, potentially creating more efficient lenses and advanced photonic circuits. From an economic

[1] VA Premnath, CH Chang - Journal of Vacuum Science & Technology B, 2023
All the authors made equal contributions in the research and experimentation processes.

perspective, efficient polymer removal techniques can reduce manufacturing costs and time, enhancing the economic feasibility of semiconductor industries and leading to new fabrication techniques. This aspect makes the research not just scientifically relevant but also commercially important. In essence, this research into polymer removal techniques provides a novel insight to nanolattice fabrication processes.

2.2 *Experimental Methodology*

2.2.1. FABRICATION PROCEDURES:

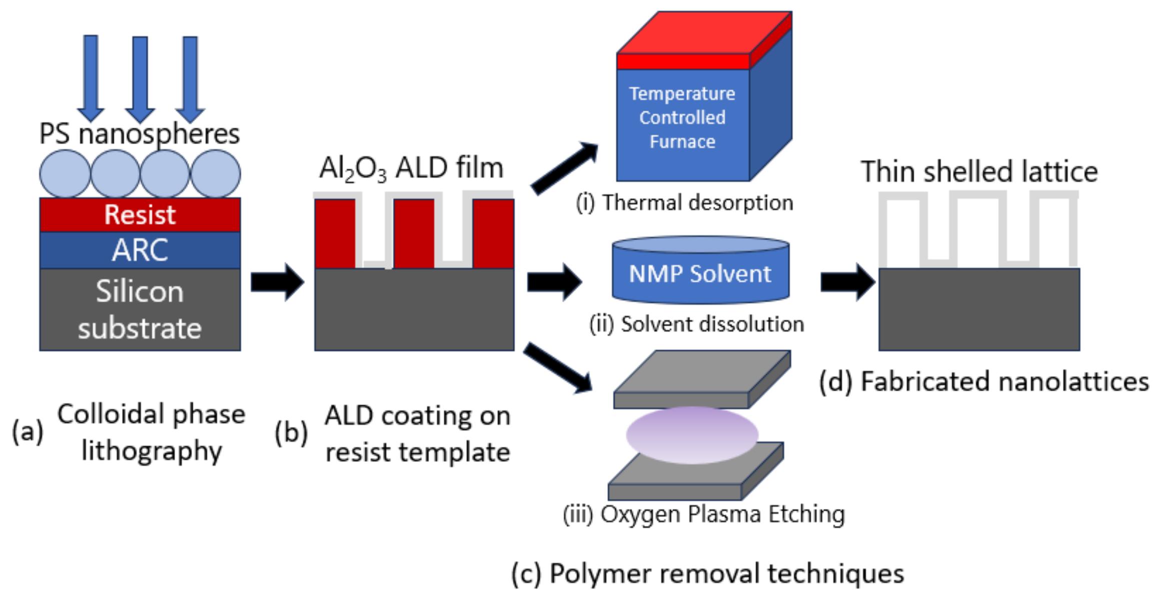

Figure 3 – Schematic of the nanolattice fabrication process involving (a) deposition of ARC, PR, and nanospheres with 500 nm diameter followed by lithography and development. (b) Samples are subjected to ALD over the template. (c) Three types of resist removal techniques include (i) thermal desorption, (ii) solvent dissolution, and (iii) oxygen plasma etching. (d) Final thin-shell lattice after polymer is removed.

The general process of fabricating complex 3D nanolattice structures is illustrated in Figure 3 and begins with a substrate stack: 100 mm silicon wafers from University Wafer,

coated with a dual-layer system. First, a 100 nm thick antireflective coating (ARC i-con-16, Brewer Science) is coated. This ARC serves a dual purpose: The first is that it prevents unwanted back reflections from the wafer surface, thereby preventing the formation of standing waves that can distort the lithographic process. Moreover, it also enhances the adhesion between the subsequent photoresist layer and the substrate itself. On top of this antireflective layer, a 300 nm thick positive-tone photoresist (PFi-88A2, Sumitomo Chemical) is deposited, and its thickness defines the pattern for subsequent lithography and development phase.

To establish the desired 3D pattern, a solution of 500 nm diameter polystyrene spheres (at 2.5% concentration, Polysciences) is assembled into a hexagonal close-packed array atop the photoresist. This array is then exposed to a 325 nm UV laser light at normal incident angle. The energy dosage, which is the amount of energy required to properly expose a photoresist material during the lithography process, is maintained at 90 mJ/cm^2, and the intrinsic optical properties of the spheres themselves lead to a 3D intensity pattern within the photoresist layer due to the light's diffraction and interference effects, as demonstrated in Figure 3(a) **[27-33].**

Following the lithography step, an ultrasonication bath is used to dislodge the nanospheres, and the photoresist is developed with a developer (CD-26, Microposit) and rinsed in de-ionized water. This sequence of actions yields a resist template that features polymer 3D nanolattices, from the intensity pattern generated during the UV exposure. The polymer templates are then subjected to an atomic layer deposition (ALD) process involving 225 cycles (Cambridge Savannah TM 200) **[34-36].** The goal is to deposit an approximately 24 nm thick Al_2O_3 coating. This is achieved through sequential half-

reactions between trimethyl aluminum (TMA) and deionized water, all taking place under a controlled atmosphere at 550 mTorr and a bed temperature of 90 °C. The outcome is a conformal Al_2O_3 layer that coats the 3D volumetric intensity patterns obtained from the lithographic process, as depicted in Figure 3(b).

The resist removal process is a critical step in the fabrication and is performed using three distinct methods as illustrated in Figure 3(c). The first method, thermal desorption, involves a controlled heating of the sample in a furnace **[39, 52].** The ramp rate of temperature increase is set to 1°C/min until it reaches 550°C, where it is maintained for 4 hours. This is followed by a gradual cooling at a rate of 5°C/min. This method ensures the complete removal of the polymer, leaving behind the Al_2O_3 structure, as shown in Figure 3(d). The second method, solvent dissolution, involves the resist polymer and ALD coated samples immersed in NMP solvent, which has high rates of resist removal. After solvent treatment, the samples are rinsed in DI water and dried. The third method, oxygen plasma etching (O_2 PE), employs a parallel plate oxygen plasma etcher to subject the samples to an environment where oxygen ions are generated and used to react with the polymer **[38, 40, 42].** This reaction converts the polymer into volatile compounds that can be evacuated from the chamber.

2.2.2. FABRICATION RESULT

The fabricated nanostructures for the three polymer template removal processes are examined using scanning electron microscope (SEM). The nanolattices post thermal desorption as shown in Figure 4, revealing the high efficiency of this method in eliminating

all traces of the polymer. Here it can be observed since there are no traces of polymer left, the obtained results from characterization techniques are highly representative of actual nanolattices, and they do not contain inclusions. Moreover, the method is capable of parallel processing since multiple samples can be contained in the furnace. The number of samples that can be contained depends on the area of the ceramic plate in the furnace. However, this thoroughness comes at the cost of time. The thermal desorption process requires a lengthy period of approximately 8 hours and 50 minutes to achieve the target temperature of 550ºC. This gradual heating rate is critical to maintain the structural integrity of the nanolattices, as rapid temperature changes could induce collapse due to the stresses imparted during the phase transition, particularly given the thin shell thickness of the lattice structure. The complexity of the process does not end there; it includes a 4-hour dwell time at the peak temperature to ensure complete evaporation of the resist material and is followed by a cooldown phase at a rate of 5ºC per minute. The complete thermal cycle thus spans about 14 hours, representing a substantial time in the manufacturing process.

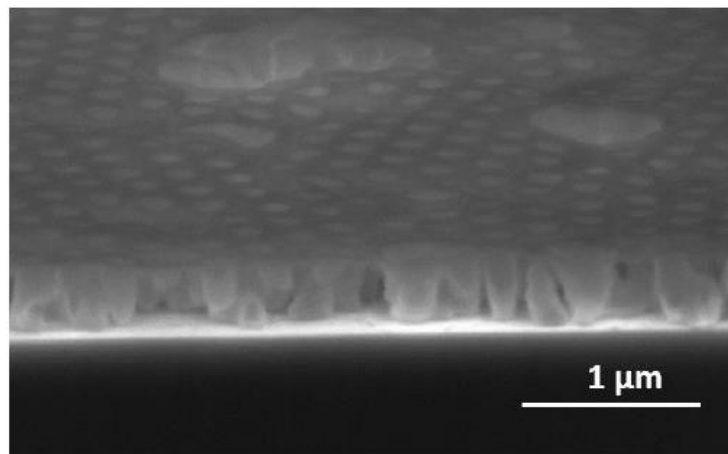

Figure 4 – Fabrication results of nanolattices after removing the polymer template in the furnace (thermal desorption). The SEM image of nanolattices fabricated with 500 nm diameter particles and 300 nm resist height.

Exploring alternatives to reduce process time, solvent dissolution presents a viable option. In this technique, samples are submerged in N-Methyl-2-pyrrolidone (NMP) for durations ranging from 5 to 15 minutes. Notably, after 15 minutes, the rate of polymer removal flattens, indicating that the remaining polymer is ensnared within the confines of the lattice, places that the solvent cannot readily penetrate. This is evidenced by the SEM images in Figure 5, where the contrast after 5 and 10 minutes of immersion in NMP is observed from the presence of residual polymer in the SEM images. Initially, the photoresist dissolves into the NMP, and upon rinsing leaves behind a porous nanolattice. The dark regions depicted after 5 minutes suggest substantial polymer presence, which diminishes substantially after 10 minutes. While NMP is highly efficient in dissolving photoresist, the nanostructure's intricacies impede the solvent's access, thus increasing the process duration. SEM provides a qualitative measure of resist presence, yet quantifying the exact amounts of residual resist remains a challenge.

The third technique, oxygen plasma etching (O_2PE), also known as ashing, introduces another method for template removal. Here, oxygen ions in a highly reactive plasma state react with the polymer and form a volatile species. This method has the advantages where solvent-based approaches fail; by being a dry etch process, it can infiltrate and navigate the 3D structures more effectively. However, its etching rate is not as high as that of NMP dissolution, possibly necessitating prolonged etch cycles for complete removal. SEM images, such as those in figure 5(e) and 5(f), show that even after 10 minutes of O_2PE, dark areas are still prominent, suggesting that the plasma was unable to clear out all the resist within the set duration. Each method, though effective, has certain inherent limitations when considered for large-scale application. Thermal desorption is precise but time-intensive; solvent dissolution has limitations with reach and permeation issues; and O_2PE, while more penetrating, is hindered by a slower etching rate. These

insights lay the groundwork for further research and development in the field, aiming to strike a balance between efficiency, effectiveness, and the practicalities of industrial scale production.

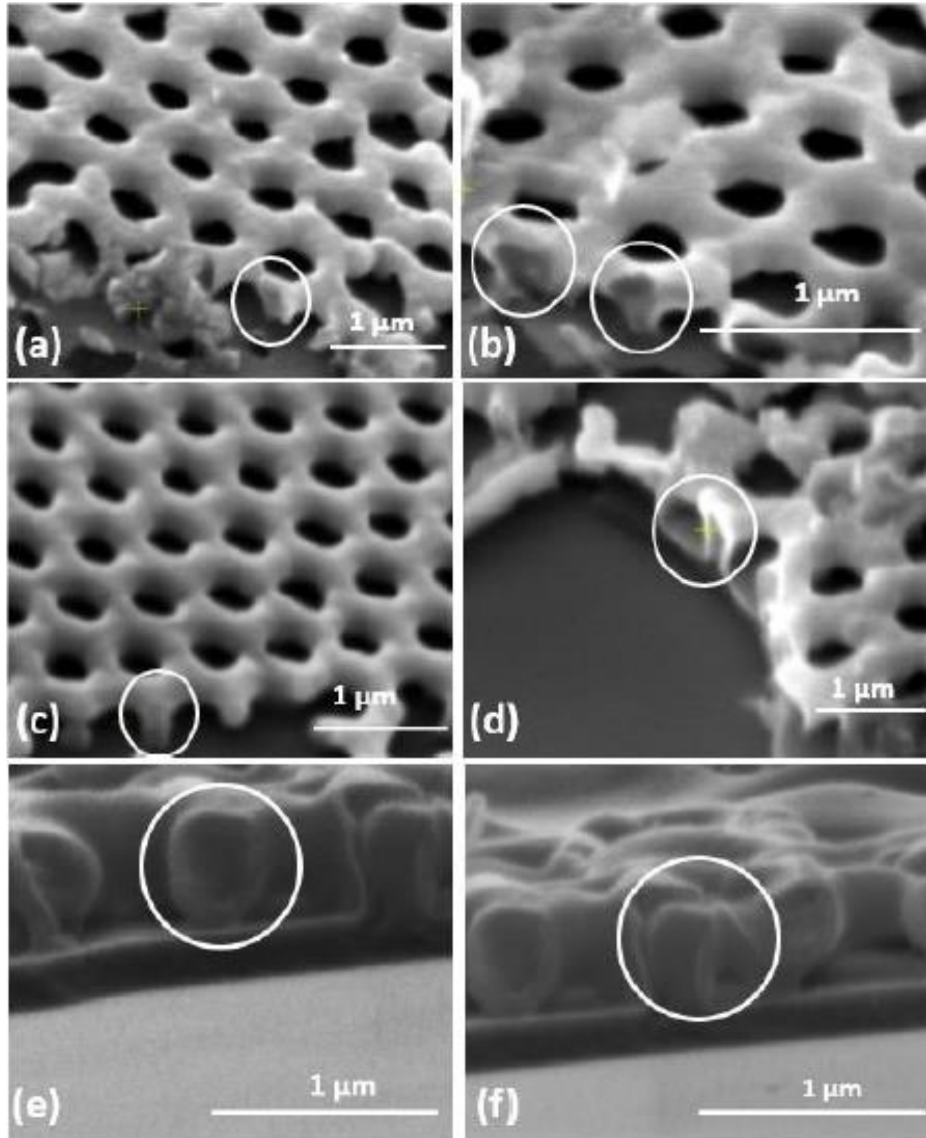

Figure 5 – Images of lattice post subjecting them to resist removal processes. (a) and (b) SEM images with prominent gray regions representing 5 min of NMP exposure, (c) and (d) images depict faint grey regions for resist removal in the nanolattices after 10 min of NMP dissolution, (e) SEM image with prominent gray regions representing 5 min of plasma etching, (f) SEM image depict milder gray regions for resist removal in the nanolattices after 10 min of the plasma etching process.

2.2.3. Optical Characterization:

The effectiveness of each resist removal method is quantitatively assessed by measuring the effective refractive indices of the resulting nanolattice films. This is carried out using spectroscopic ellipsometry (SE), an optical technique that analyzes the change in polarization of light upon reflection or transmission through the sample. SE measures two parameters: the amplitude ratio (Ψ) and the phase difference (Δ) of the two orthogonal polarizations, and the data obtained is then fitted to theoretical models through regression analysis to extract information about the film's refractive index and thickness **[53].**

In this study, the SE measurements span a wavelength range from 200 to 1600 nm. The model used for the nanolattice layer assumes an isotropic Cauchy layer, where the refractive index is consistent in all directions and haves as a dielectric. The Cauchy model is layered over a native oxide layer, which is iteratively fitted for its thickness to accurately represent real-world conditions where a native oxide layer may naturally form on the silicon surface. For samples processed with NMP and O_2 plasma etching, an additional ARC layer is factored into the SE model to account for the alterations to the optical properties of the structure.

This fabrication process, along with the accuracy of the SE characterization, is what allows for the creation of functional nanolattice structures. These structures are anticipated

to have significant applications in the field of photonic devices, where their unique optical properties can be used to improve the performance of various optoelectronic components.

2.3 *Results and Discussion*

2.3.1. SPECTROSCOPIC ELLIPSOMETRY MEASUREMENTS:

Expanding upon the initial methodology for analyzing the residual polymer in the nanolattice samples using spectroscopic ellipsometry (SE), the process begins with the obtaining empirical data which consists of the interaction of polarized light with the sample's surface. This interaction is characterized by changes in the amplitude ratio (Ψ) and the phase difference (Δ) of the reflected light, which are measured across a spectrum of wavelengths, as depicted in Figure 6(a), while 6(b) depicts the model used consisting of layers of silicon, silicon dioxide, and an isotropic Cauchy layer. By employing an optical model, these measurements are translated into a quantitative assessment of the physical properties of the sample, such as the thickness of the nanolattice and its refractive index. This is particularly relevant for samples that have undergone the thermal desorption process.

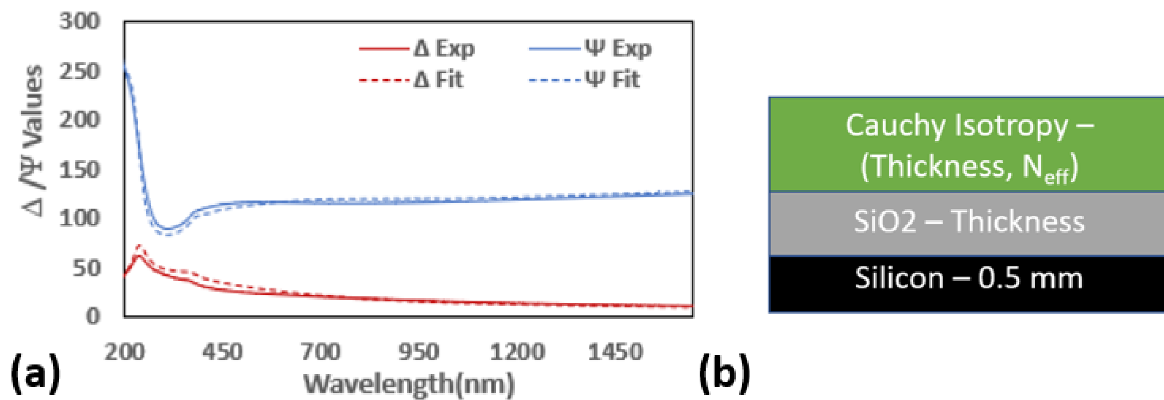

Figure 6 – Measured and fitted Δ/Ψ values over the wavelength spectrum for a nanolattice sample subjected to thermal desorption. The close agreement between the two indicates that the measured effective index is accurate.

The model's accuracy is fine-tuned through an iterative fitting process, aimed at minimizing the mean square error (MSE) between the empirical data and the model's predictions. The process computationally tries to match the modeled parameters with the experimentally derived data. This iterative process continues until the optical model mirrors the measured characteristics of the film stack with low MSE. For the sample that was subjected to thermal desorption, the optimized MSE stands at a notable 23.1 (Deviations from perfect structures in terms of mean square error). This contrasts with the samples that have been processed using NMP and O_2Plasma Etching (O_2PE), which recorded higher MSE values of 54.8 and 42.4, respectively as shown in Table 1. These elevated MSE figures could be indicative of a less uniform removal of the polymer, suggesting that remnants of the material persist within the nanolattice to a greater degree than with thermal desorption. Such disparities underscore the heightened precision and effectiveness of the thermal desorption technique in eradicating the polymer template, which is corroborated by a lower MSE value, signifying a more homogenous and complete removal of the resist. This analytical approach underscores the critical importance of a thorough and uniform template removal process to ensure the integrity and uniformity of the resultant nanolattice structures.

2.3.2. CHARACTERIZATION OF RESIDUAL RESIST:

The refractive index of a material, as measured by spectroscopic ellipsometry (SE), is a critical parameter in determining the presence and amount of polymer resist remaining

in nanolattice films. This index indicates the interaction of light when passing through a material, and it is highly sensitive to the material's composition and structure. When nanolattice films are subjected to template removal processes such as thermal desorption, solvent dissolution with N-methyl-2-pyrrolidone (NMP), or oxygen plasma etching (O_2 PE), the removal of polymer resist alters the film's composition, consequently changing its refractive index. A lower refractive index typically suggests that a significant amount of resist has been removed, reducing its contribution to the overall material composition. Conversely, a higher index indicates a greater presence of resist, implying less effective removal. Therefore, by monitoring the variations in the refractive index through SE, it's possible to assess the effectiveness of the template removal processes in extracting polymer resist from the nanolattices. Thus, the refractive indices of the nanolattice films provide critical insight into the effectiveness of the three distinct template removal processes. In Figure 7(a), the SE data plot the measured effective refractive indices against the treatment time, showcasing how these indices evolve as the polymer is gradually removed from the nanolattices.

For the thermal treatment process, the measured refractive index reaches 1.0661, significantly lower than the index of Al_2O_3. This lower index is indicative of the high porosity achieved due to the complete removal of polymer residues. The absence of polymer is verified by the fact that this value serves as the reference line, demarcated with a dashed line in the graph. The thermal process, despite its long duration, exceeding 14 hours, sets the benchmark for the cleanest removal **[52],** though its lengthy nature raises questions about its practicality for large-scale or time-sensitive applications.

With regards to the chemical process with NMP, SE shows that the refractive index of the untreated nanolattice starts at 1.7023, which encompasses the composite material of both Al_2O_3 atomic layer deposition (ALD) and the photoresist material. Upon initiating the NMP treatment, the index sees a substantial drop to 1.2364 after just 5 minutes, suggesting a rapid dissolution of the photoresist. This is faster than the O_2 PE process, which after the same period, only reaches an index of approximately 1.4281. Such data imply a more efficient polymer clearance by the NMP solvent, likely due to its lower viscosity which enables it to penetrate and dissolve the polymer more effectively within the nanolattice's confines. The optical properties continue to change as the treatment time extends. After 10 minutes, the indices for NMP and O_2PE treatment processes plateau to 1.1784 and 1.2596, respectively. Following a 15-minute treatment period, the SE readings stabilize further, culminating in final refractive indices of 1.1336 for NMP and 1.1536 for O_2PE. Despite these reductions, the indices do not reach the baseline established by the thermal process, signifying the persistence of residual polymer within the structures treated by NMP and O_2 PE. Tables 1(a) and 1(b) represent the variation in refractive indices with increasing times of exposure to resist removal processes such as NMP and O_2PE.

Time	Wavelength	Nx	Ny	Nz	Isotropic Index	MSE values
0 mins	633.43	1.6974	1.6974	1.6984	1.7023	41.7
5 mins	633.43	1.5121	1.5121	1.5133	1.4281	39.8
10 mins	633.43	1.2625	1.2625	1.2635	1.2596	44.2
15 mins	633.43	1.1629	1.1629	1.1639	1.1536	43.9

Table 1 – Variation of indices and MSE values of lattices with increase in time of exposure for 0, 5, 10 and 15 minutes, when subjected to NMP solvent

Time	Wavelength	Nx	Ny	Nz	Isotropic Index	MSE values
0 mins	633.43	1.6974	1.6974	1.6984	1.7023	52.7
5 mins	633.43	1.2353	1.2353	1.2366	1.2364	51.3
10 mins	633.43	1.1674	1.1674	1.1682	1.1784	55.8
15 mins	633.43	1.1445	1.1445	1.1455	1.1336	59.4

Table 2 – Variation of indices and MSE values of lattices with increase in time of exposure for 0, 5, 10 and 15 minutes, when subjected to O_2PE process

2.3.2. THEORETICAL VALIDATION OF RESIDUAL RESIST:

Through the lens of effective medium theory, these measured indices are employed to ascertain the volume fraction of residual resist. The Maxwell-Garnett (MG) model, which conceptualizes the Al_2O_3 ALD and polymer as inclusions within an air host medium, is employed to compute this fraction **[54].**

$$\frac{n_{\mathrm{eff}}^2 - n_{\mathrm{air}}^2}{n_{\mathrm{eff}}^2 + 2n_{\mathrm{air}}^2} = f_{ALD}\left[\frac{n_{\mathrm{ALD}}^2 - n_{\mathrm{air}}^2}{n_{\mathrm{ALD}}^2 + 2n_{\mathrm{air}}^2}\right]$$

For thermal desorption, the polymer's complete removal simplifies the system to two phases, allowing for a straightforward application of the MG equation. With the refractive index of air (n_{air}) as 1, the Al_2O_3 index (n_{ALD}) at 1.77 for a wavelength of 632 nm, and the effective index at 1.0661, the volume fraction of Al_2O_3 (f_{ALD}) is computed to be approximately 10.4%. This calculated f_{ALD} becomes a point of reference for all nanolattice samples since identical photoresist templates and ALD thicknesses are employed across the board **[54].**

$$\frac{n_{\mathrm{eff}}^2 - n_{\mathrm{air}}^2}{n_{\mathrm{eff}}^2 + 2n_{\mathrm{air}}^2} = f_{\mathrm{ALD}}\left[\frac{n_{\mathrm{ALD}}^2 - n_{\mathrm{air}}^2}{n_{\mathrm{ALD}}^2 + 2n_{\mathrm{air}}^2}\right] + f_{\mathrm{resist}}\left[\frac{n_{\mathrm{resist}}^2 - n_{\mathrm{air}}^2}{n_{\mathrm{resist}}^2 + 2n_{\mathrm{air}}^2}\right]$$

When assessing the NMP and O_2 PE-treated samples, a third phase (the residual photoresist) must be accounted for, introducing additional complexity into the MG model. Here, the volume fraction of the resist (f_{resist}) and its refractive index (n_{resist}) at 1.6560 at 632 nm are introduced into the MG equation. Despite this complexity, the application of the model unveils that at the onset of the resist removal process (0 minutes), an overwhelming majority of the resist, approximately 89.2%, is present as represented in figure 7(b). This figure dramatically decreases with NMP dissolution to 24.2%, 14.9%, and finally 7.3% at 5, 10, and 15 minutes, respectively. In the case of O_2PE, the resist volume fraction similarly diminishes to 62.1%, 28.2%, and 10.7% at the corresponding time intervals. These reductions show NMP's superior efficacy in stripping the polymer compared to O_2 PE. Despite these detailed findings, the accuracy of the SE-based quantification approach is not without limitations. Variations in the nanolattice geometry, such as those due to the colloidal assembly defects, or structural collapses, can significantly show differences between the true values of indices and the SE measurements. Moreover, the non-uniformity of polymer removal, often initiating at the nanolattice's outermost layers and progressing inward, leads to an underestimation of the remaining polymer's volume fraction. This is evident in the SEM images from Figure 5 where the core of the nanolattices retains dark post-treatment. This shows that the notion that these remaining resist portions are more challenging to eliminate. The surface roughness of the nanolattices is another factor that influences the SE measurements. With the O_2 PE process, a gradual increase in roughness is noted, likely due to the etching mechanism which attacks the polymer at a microscopic level. This roughness results in increased scattering losses in the SE data, potentially

complicating the interpretation of the refractive indices and, by extension, the calculated polymer volume fractions. In conclusion, the combined SEM and SE analyses provide an effective characterization of the three polymer removal processes, each with their unique advantages and limitations. While thermal desorption has the most resist removal, its slow nature shows that NMP dissolution as a viable, more rapid alternative, despite incomplete resist removal. O_2 PE's moderate resist removal rates and lesser time than desorption displays that there are possible combinations of these parameters that can be optimized to improve between resist removal rates and process times. The future work on this research would lie on balancing the trade-offs between treatment duration, structural integrity, and polymer removal completeness, a three-parameter variation, which is critical to the advancement of refining the lattice fabrication process.

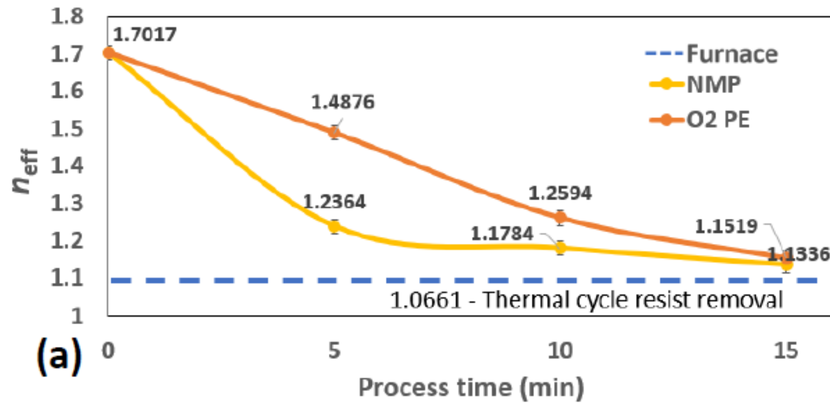

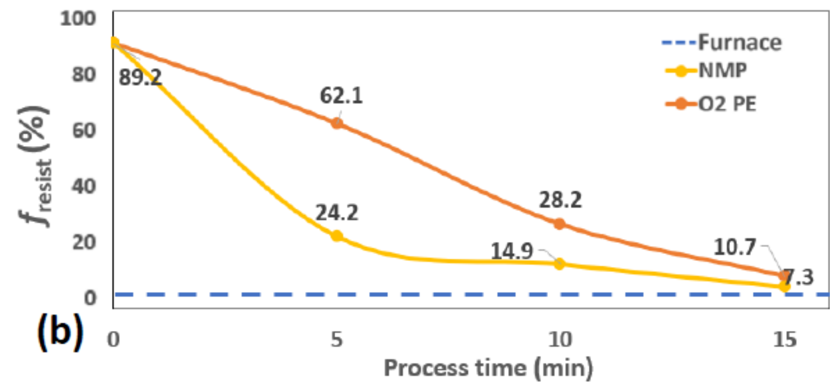

Figure 7 – (a) Measured effective refractive indices of the nanolattice vs process time. (b) Calculated volume fraction of residual polymer vs process time using the MG model.

2.4 *Conclusion*

This research delves into the efficiency of different resist removal techniques in the fabrication of porous nanolattices, focusing on thermal desorption, NMP dissolution, and O_2 plasma etching. Each method's impact on the final nanolattice structure is analyzed, revealing the advantages and limitations. The thermal desorption process, involving heating the samples to 550 ℃, proves to be the most effective in eliminating polymer residues, as evidenced by the lowest measured effective refractive index of 1.0661. This indicates almost complete polymer removal, resulting in highly porous structures. However, the process is time-intensive, exceeding 14 hours, which could be a limiting factor in rapid production scenarios. In contrast, NMP dissolution offers a faster alternative. After a 15-minute treatment, the nanolattices exhibit an effective index of 1.1336, corresponding to a residual polymer volume of approximately 7.3%. This method's efficiency is attributed to NMP's solvent properties, facilitating quicker polymer dissolution than O_2 PE. O_2plasma etching, while being a dry etching process, shows a slower rate of polymer removal. The method resulted in nanolattices with an effective index of 1.1536 and a higher residual polymer volume of 10.7%. This indicates that while O_2PE is effective, it doesn't quite match the efficiency of NMP dissolution.

Applying the Maxwell-Garnett (MG) model, these indices and volumes provide insight into the nanolattices' porosity and composition. The findings from this study have significant implications for the fabrication of nanolattices. They contribute to the advancement of nano-architected materials and their applications in various fields like

nanophotonics, where control over material porosity and structure is crucial. Overall, this research highlights the importance of choosing the appropriate resist removal technique based on the specific requirements of the nanolattice fabrication process, balancing efficiency, and structural integrity.

CHAPTER 3: FABRICATION OF THREE-DIMENSIONAL OPAL NANOLATTICES USING TEMPLATE-DIRECTED COLLOIDAL ASSEMBLY[2]

3.1 *Introduction*

Inverse opaline structures are fascinating and intricate materials characterized by a unique arrangement of voids and solid phases, essentially the reverse of a natural opal's structure. In natural opals, spheres of silica are closely packed, creating a specific interaction of light and color. Inverse opals, on the other hand, have a lattice of voids where these spheres would be, surrounded by a solid material. This results in a structure with a regular, repeating pattern that affects light in unique ways, making them highly valuable in photonic applications for manipulating light. Nature offers several examples of inverse opaline nanostructures. For instance, certain butterfly wings exhibit brilliant colors not from pigments, but from microscopic structures that resemble inverse opals. These structures manipulate light through diffraction, resulting in vivid colors that can change with the angle of view. Similarly, the structural coloration in the feathers of some birds and the scales of certain beetles is due to inverse opaline structures.

This chapter presents a technique for creating three-dimensional (3D) inverse opal nanostructures, which are integral to advancements in nanophotonics, laser technology, and optical systems. The method employed is colloidal lithography, which patterns a hexagonal closed packed hole array **[32,33].** These holes guide the assembly of colloidal particles into 3D configurations. This method ensures that the 3D opal structures are in precise alignment with the two-dimensional (2D) hole array. Such alignment is beneficial for enhancing

---

[2] VA Premnath, I Chen, KC Chien, CH Chang - Journal of Vacuum Science & Technology B, 2022
All the authors made equal contributions in the research and experimentation processes.

coherence and minimizing structural defects. The process involves using polymer patterns as a temporary framework for atomic layer deposition (ALD), facilitating the creation of intricate nanolattices **[34-36].** The nanolattices are then overlaid with opal structures through controlled ultrasonication. The resulting nanostructures are characterized by their high porosity, a vital feature for developing materials with low refractive indices essential in nanophotonics. A substantial layer of titanium oxide, which has high refractive index, is subsequently deposited on the nanolattices. This addition showcases the mechanical resilience of the structures beneath. These precisely engineered nanolattice structures, with their carefully controlled heights, have potential applications for use as low-index layers in various applications. Their suitability extends to devices such as Bragg reflectors, further nanophotonic applications, and in the construction of optical multilayer systems.

3.2 *Fabrication Procedure*

The detailed schematic of the fabrication method for creating three-dimensional (3D) nanolattice structures with integrated hollow opal formations is systematically illustrated in Figure 8. The procedure starts with 100 mm silicon substrates sourced from University Wafer. These are spin-coated with a 100 nm layer of anti-reflection coating (ARC i-con 16, Brewer Science) followed by a 300 nm layer of positive-tone photoresist (PFi-88A2, from Sumitomo Chemical). The ARC serves a dual purpose: it mitigates back reflections from the silicon wafer surface, thus reducing the formation of standing waves that can hinder the photolithography process, and it enhances the adhesion between the photoresist layer and the substrate, ensuring structural integrity throughout the process.

Subsequently, polystyrene (PS) nanospheres, each with a diameter of 500 nm (2.5% solids concentration, from Polysciences), are self-assembled on the photoresist-coated wafer, as depicted in Fig. 8(a). This assembly forms a hexagonal close-packed array, a configuration that naturally minimizes surface energy **[56].** The spheres are employed as near-field phase shift masks. Following this, the arrangement is exposed to the helium-cadmium (HeCd) ultraviolet laser (manufactured by Kimmon, emitting at a wavelength of 325 nm) with an energy dose calibrated to 110 mJ/cm^2. This exposure step creates a volumetric intensity pattern in the photoresist layer underneath, a direct consequence of the Talbot effect **[55].** The nanospheres are then removed via an ultrasonication bath. The photoresist beneath is developed for 60 seconds using a developer (CD-26, from Microposit) , ultimately yielding a periodic array of holes as shown in Figure 8(b). The development stage allows for the opportunity to remove the nanospheres partially using ultrasonication, as illustrated in Figure 8(c). By fine-tuning the colloidal solution concentration and the assembly process parameters, we can accurately control the assembly of discrete PS nanosphere layers on the photoresist template.

These photoresist structures with PS nanospheres then act as a sacrificial template for the subsequent atomic layer deposition (ALD) **[34-36].** The process employs a commercial ALD system (Cambridge Savannah TM 200) to deposit a conformal Al_2O_3 layer on the photoresist and PS surfaces, as shown in Fig 8(d). This Al_2O_3 formation is achieved through sequential self-limiting half-reactions involving trimethyl aluminum (TMA) and deionized water. The precise ALD cycle recipe used is sequenced as 0.025/10/0.025/20 seconds for TMA exposure, nitrogen purge, water exposure, and a final nitrogen purge, respectively. Each cycle incrementally contributes a 0.1 nm thickness to the Al_2O_3 layer. The deposition is conducted at a pressure of 550 mTorr and a substrate temperature of 90°C. A total of 200

ALD cycles are performed to achieve a final coating thickness of 20 nm, enabling the photoresist to function effectively as a sacrificial template for the nanolattice structure. To prepare for the addition of subsequent layers and to ensure an even coating surface, the nanolattice is planarized with another spin-coated layer of PFI 88 photoresist, approximately 350 nm in thickness. This planarization process is critical to provide a stable base and to prevent infiltration of TiO_2 into the nanolattice during the subsequent deposition step. After planarization, a solid TiO_2 layer is deposited onto the surface using an electron-beam evaporator (Kurt J Lesker PVD-75), with a deposition rate of about 0.26 nm/s at an operating voltage of 6000 V. The total thickness of the TiO_2 deposition is maintained at 80 nm to ensure a substantial capping layer is formed over the planarized surface, as showcased in Fig. 8(e).

The final structural integrity is achieved by baking the structure at a precise temperature control sequence. The temperature is elevated to 550°C at a rate of 1°C per minute, where it is held for 30 minutes to ensure thorough removal of the photoresist and PS template. Subsequently, the temperature is methodically lowered to 50°C at a cooling rate of 5°C per minute. Post this thermal processing cycle, the resultant structure comprises a stack of the Al_2O_3 nanolattice and hollow opal formations, as visualized in Fig 8(f). The TiO_2 layer, now capping the stack, is instrumental for the integration of additional materials onto the porous nanostructures, completing the fabrication process for these advanced 3D nanolattices.

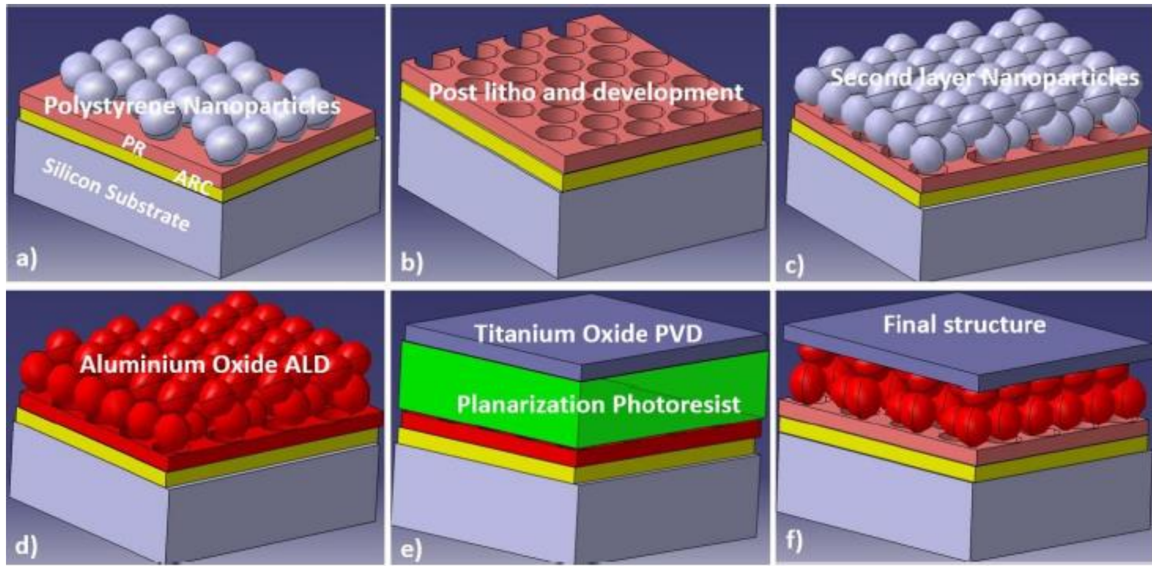

Figure 8 – Fabrication process for hollow opal nanolattice. a) deposition of ARC and PR layers on silicon substrate over which the nanospheres are transferred manually. b) Exposure and development of photoresist. c) Assemble additional PS nanospheres on the photoresist template. d) Deposit conformal ALD coating on polymer nanostructures. e) Planarization coating of PR and deposit TiO_2. f) Removal of PR and buffer layer by temperature treatment.

3.3 *Results and Discussion*

3.3.1. PATTERNING OF RESIST USING UV LITHOGRAPHY:

Lithography is an important fabrication technique in the microfabrication and nanofabrication industries. At its core, lithography is the process of transferring a pattern from a photomask to a light-sensitive photoresist material applied on a substrate, such as a silicon wafer. The process begins with the application of the photoresist on the substrate, which is then pre-baked to remove any solvent and solidify the film. Next, the substrate coated with the photoresist is exposed to ultraviolet (UV) light through a photomask, which contains the desired pattern. The photomask blocks light in certain areas and allows it to

pass through others. The cross-section views and top views of the 2D array of holes patterned into a photoresist as a template for the directed assembly of polystyrene (PS) nanospheres is depicted in the SEM images in Figure 9. The uniform distribution of the hexagonal close-packed (HCP) order is observed, despite the challenges inherent to colloidal assembly, even though the structures exhibit small spatial-phase coherence and form multiple grain boundaries. These features are characteristic of the colloidal assembly, indicating that while control is exerted over the process, stochastic elements inherent to particle interactions still play a significant role.

The control over exposure to an optimized 100 mJ/cm^2 dose followed by ultrasonication to remove the particle showcases an intricate balance between etching and preserving the photoresist template's integrity. The top-view SEM image after development (Figure 9(a)) reveals not just the uniformity across the vast array but also the minute imperfections that emerge as point and assembly defects. These defects, while minor, underscore the criticality of particle size uniformity – a challenging parameter when working at the nanoscale, where even a 5% variance can have noticeable impacts on the overall assembly **[56].**

Delving deeper into the cross-sectional analysis, Figure 9(b) provides a view of the homogeneity in pattern dimensions and hole depth. At a microscopic level, this uniformity is high given that it reflects the photoresist thickness and defines the subsequent nanostructures' dimensions. However, the assembly defects are due to variability in nanosphere sizes and the limitations of current colloidal assembly techniques. The occasional impurities and inclusions, despite cleaning with oxygen plasma, introduce

complexity into the fabrication process, leading to voids and the potential for crack development in the particle arrangement.

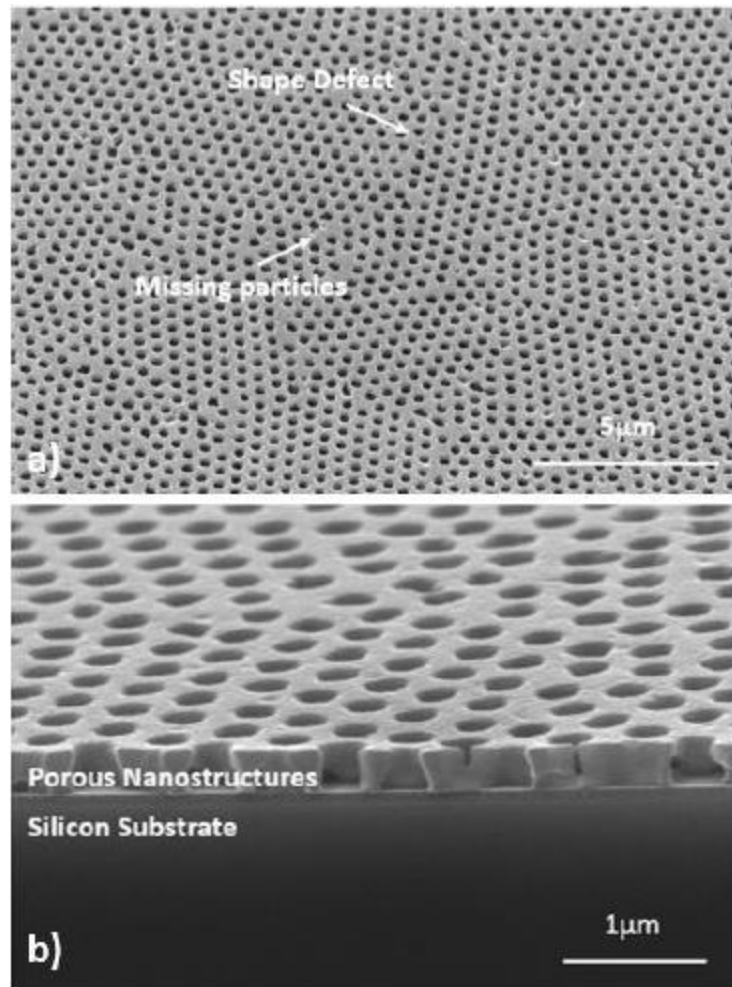

Figure 9 – Cross-sectional SEM images of fabricated photoresist template. a) Top view of patterned photoresist after exposure and development. b) Side view of patterned resist exposed from the uniform hexagonal closed packing of nanospheres.

3.3.2. FORMATION OF MULTILAYER INVERSE OPAL STRUCTURES:

The evolution of this template into a three-dimensional structure by assembly of PS nanospheres is a multiphase process involving ultrasonication of the nanospheres to remove specified amounts, and followed by a drying process that encourages the nanospheres to nestle into the resist template holes. This process, which must be controlled, lays the foundation for the creation of additional layers, with the potential to stack 2-4 layers as the particle concentration increases. The subsequent steps involve planarization with a thick photoresist and a uniform coating of TiO_2. The annealing process, tuned at 550 ºC with a ramp-up rate of 1°C/min, ensures the thorough removal of the sacrificial photoresist and PS layers. This step involves the removal of the resist, which finally leads to the formation of tangible in the form of 3D opal structures showcased in Figures 10(a) and 10(b). Here, the SEM images reveal the presence of a porous nanostructure around 300 nm thick.

These structures have a high quality in their functional phase alignment to the underlying porous nanostructures, because of the template-directed assembly. The opal layer's height, which is about 500 nm, determined by the diameter of a single layer of nanospheres, leads to a layered, yet uniform, deposition of an 80 nm TiO_2 layer, on top of the 3D nanostructures. This final layer introduces an additional refractive index interface between the low-index Al_2O_3 opal nanolattices and the high-index solid TiO_2 film.

The refractive index mismatch between the materials is strategic choice to enhance the reflectivity of structures, since there are air gaps in the inverse opal structures that result in higher mismatch. These gaps, residues of the inverse spheres' voids, contribute to an increase in the overall index mismatch.

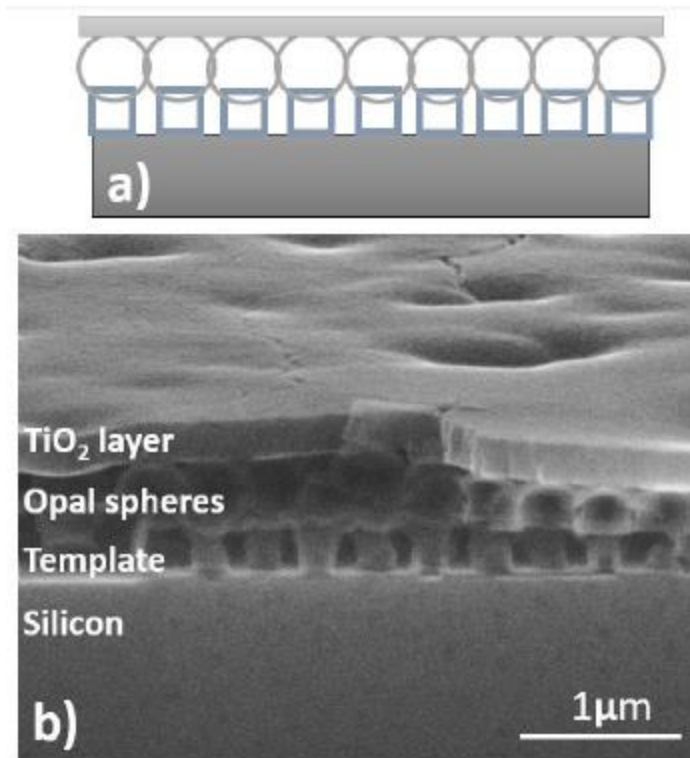

Figure 10 – Illustration of proposed high porosity opal nanostructure with capping film to create a high index mismatch interface. The schematic a) depicts a stack of desired nanostructure consisting of silicon substrate, porous Al_2O_3 nanostructures, hollow opal nanostructures, and a solid TiO_2 layer. b) represents the SEM image of the fabricated sample depicting the stacking of nanostructure.

The research about the inverse opal structures shows interesting insights into the relationship between the number of colloidal assembly layers and the resultant structure's height. Figure 11 shows cross-sectional SEM images which show a direct correlation: as the assembly layers increase from one to four, the thickness of the porous 3D nanostructures correspondingly swells from 500 nm to a significant 2000 nm. This height increase, achieved through manipulation of the PS nanosphere concentration in the aqueous solution, is important in broadening the optical bandgap of the materials. However, precision in the

ultrasonication method is wanting, with inconsistencies leading to regions of varied layer numbers, an issue that ongoing research into layer-by-layer assembly aims to refine.

The height of these 3D nanostructures, coupled with their lattice geometry and the applied ALD thickness, provides the ability to modulate the film's effective refractive index with finesse. This control over the optical path length within the nanostructures facilitates the tailoring of photonic crystal reflectors across a wider wavelength spectrum. The anisotropic nature of nanolattice results in distinct optical properties depending on the light's polarization direction. Yet, with increased structural height comes a trade-off: the potential decline in mechanical stability due to the weight leading to the sagging of layers **[57].** This is evidenced by the increasing surface undulation with each added opal layer, which not only reflects the increased presence of assembly defects but also suggests a higher deviation in refractive index across the surface. The SEM images depict a pronounced deformation in the bottom layer of the nanolattices, a result of the structural collapse under thermal cycling. This collapse, as the photoresist transitions through its phases during polymer evaporation, introduces surface tension that warps the designed lattice architecture, reducing the expected thickness. The underlying anti-reflective coating (ARC) worsens this effect, altering phase at elevated temperatures and contributing to the sinking of the structure.

Moreover, the sagging of the TiO_2 top layer into the voids left by the opal structures results in point contacts that encourage further deformation. This is even increased during electron-beam evaporation and baking processes designed to remove residual resist. The results because of this lead to reduction in reflectance values, since periodicity that defines the photonic structure's reflective properties is diminished.

Mechanical stability degrades with the addition of layers, a phenomenon attributed to the thermal cycle required to remove all polymer components, including PR, PS, and ARC. The transformation of these materials into liquid and then vapor not only poses a risk of structural collapse due to uneven surface tension but also threatens the uniformity of the nanolattice's thickness and the strength of the porous layers. Escape routes for the vaporizing photoresist become less with increased layering, a situation that might be made better with a thicker ALD application for reinforced structural rigidity. Yet, ALD's inability to deposit at nanosphere contact points means that post-evaporation, the voids left behind become more prevalent with each layer, weakening the overall mechanical framework. In the four-layer structure, these voids are markedly noticeable, with a corresponding increase in contact points between spheres leading to an increase in potential structural failure points. This is depicted in both Figures 10 and 11, where the SEM images reveal the volumetric increase in voids increase with the layer count.

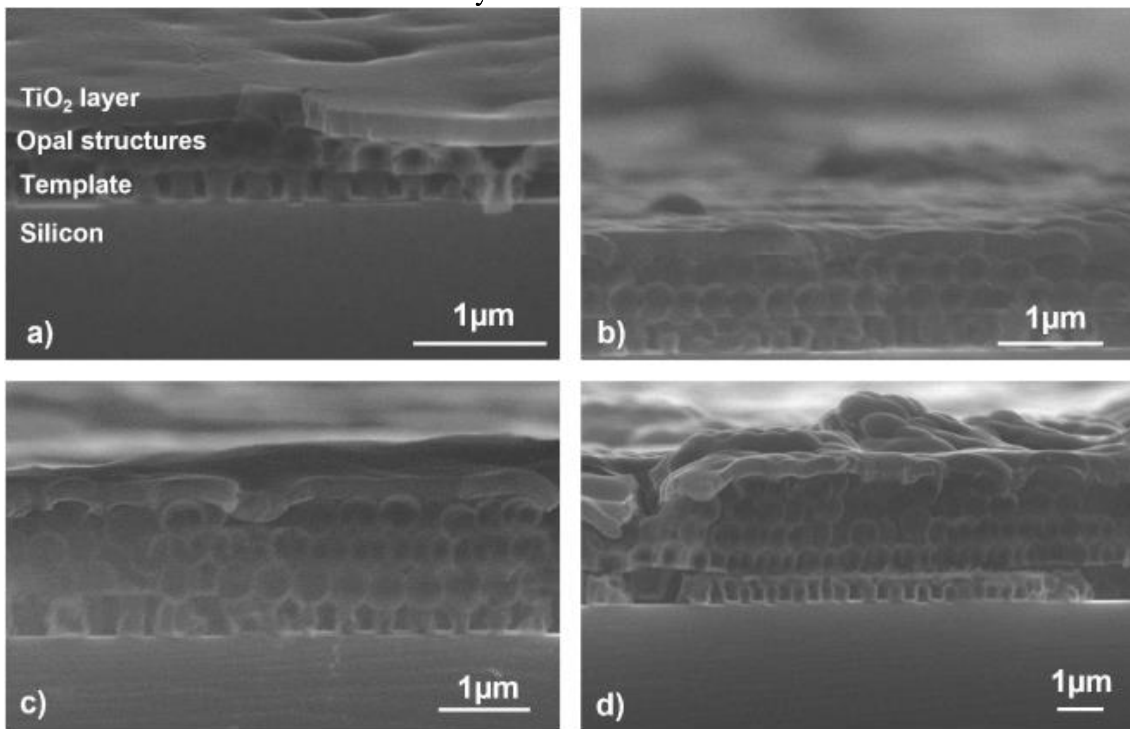

Figure 11 – SEM images of fabricated opal nanostructures containing a) single, b) two, c) three, and d) four nanosphere assembly layers prior to deposition of ALD film.

3.3.3. FABRICATION ISSUES:

The formation of cracks in the uniform titanium dioxide (TiO_2) film layer, as depicted in Figure 12, presents a notable aspect of the study. These cracks vary in size, ranging from the macroscale down to the microscale. The widest of these cracks measure in the order of several micrometers, while the narrowest are approximately 300 nanometers wide. This phenomenon can be attributed to a couple of primary factors. Firstly, the mechanical instability of the structure plays a significant role. This instability arises due to variations in height during the thermal cycles implemented to remove polymers from the structure. The heating and cooling processes induce stress within the TiO_2 layer, which, due to its rigidity and the variances in structural height, results in the formation of these cracks. The second factor contributing to the crack formation is the mismatch in the coefficient of thermal expansion (CTE) between TiO_2 and aluminum oxide (Al_2O_3). TiO_2 has a CTE value of approximately 8.4×10^{-8} per Kelvin, whereas Al_2O_3 has a CTE of about 4.5×10^{-8} per Kelvin. This difference in CTE values leads to different expansion and contraction rates between these two materials when subjected to high temperatures, particularly noticeable at the peak temperature of 550°C during processing. The resulting strain from this mismatch is a significant contributor to the development of cracks.

Other minor factors that may contribute to crack formation include inclusions on the wafer surface, voids within the material, and assembly defects. Despite the presence of these cracks, which introduce variations in the refractive index between high and low

values, the overall mechanical stability of the structures remains largely unaffected. This resilience suggests that while the cracks impact certain optical properties, they do not compromise the structural integrity of the TiO_2 films in significant ways. Such insights are critical for understanding and improving the fabrication process of these nanostructured materials.

Although these cracks may introduce refractive index variations, the overall mechanical stability appears uncompromised.

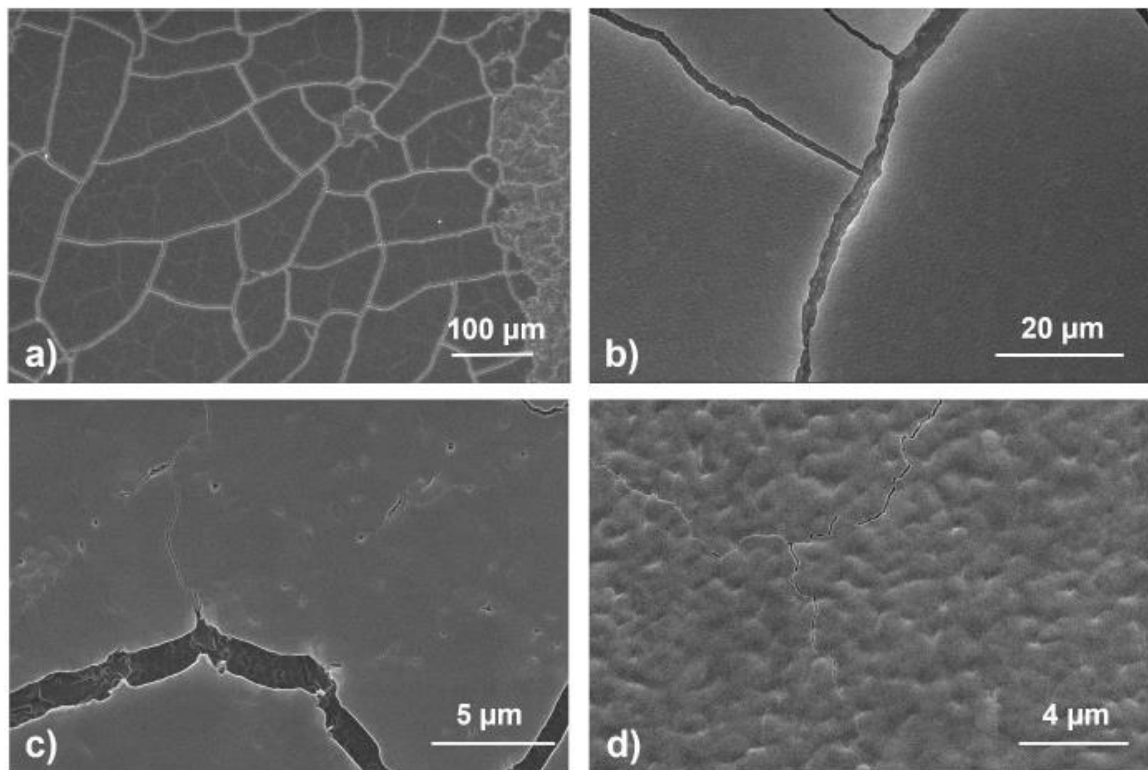

Figure 12 – SEM images of fabricated structures consisting of macro and microcracks with a) low magnification of 100 µm scale bar and b) higher magnification of 20 µm scale bar. c) Primary micro crack formation over the titanium oxide layer and d) branched microcracks from the primary microcracks which have thickness in the order of 300 nm.

A particular issue arises when the intended hexagonal close-packed (HCP) structures, which are crucial for optimal material properties, develop particle arrangement defects as in Figure 13. Ideally, in an HCP structure, particles are tightly packed in a repeating hexagonal pattern, maximizing density and structural efficiency. However, deviations from this arrangement can occur, leading to compromised structural integrity and altered material properties. These defects in the particle arrangement can stem from various factors, including inconsistencies in particle size, shape, and the precision of assembly processes and the SEM image of resulting deviations is shown in Figure 13 (b).

Another notable factor contributing to the disruption of the HCP structures is the presence of dust and other minute contaminants as shown in figure 13(a). During the assembly process, dust particles can settle onto the developing nanolattice, disturbing the formation of the perfect hexagonal pattern. These dust particles can significantly impact the neighboring arrangement of particles. They act as physical barriers, preventing the colloidal particles from settling into their intended positions and forcing them into irregular arrangements. This disruption can lead to localized areas within the nanolattice where the desired HCP structure is not achieved, resulting in variations in mechanical and optical properties across the material. The presence of such defects highlights the importance of maintaining a clean, controlled environment during nanolattice fabrication. Minimizing exposure to airborne contaminants, implementing precise control over particle deposition, and ensuring uniformity in particle size and shape are crucial for achieving the desired HCP structures. Addressing these challenges is vital for the advancement of nanotechnology applications, where the integrity of such structures plays an important role in determining material performance.

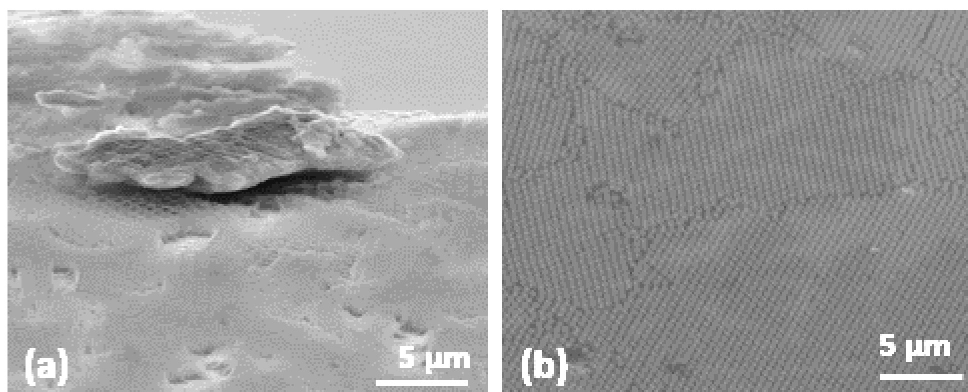

Figure 13 – SEM images of patterned structures showing the (a) presence of dust particles on the structures, resulting in disrupted HCP formation in the neighboring zones, and (b) particle arrangement defects that arise from inherent shape and size defects in individual spherical nanospheres.

3.4 *Conclusion*

During this investigation, a novel methodology was employed to synthesize three-dimensional opal nanostructures with varying layers, specifically one to four, utilizing a two-dimensional nanohole array as a foundational template. This approach utilizes the principles of template-directed assembly, with polystyrene (PS) nanospheres to construct opal structures that are spatially-phase aligned with the photolithographically patterned features beneath. These polymer-based nanostructures serve a crucial role as templates for atomic layer deposition (ALD), facilitating the formation of self-supporting Al_2O_3 hollow opal structures after a carefully regulated thermal cycle. The thickness of the resulting discrete nanostructure layers is modulated by adjusting the concentration of nanospheres during the assembly process, enabling precise control over the overall thickness. While augmenting the number of opal layers leads to increased nanolattice heights that enhances

photonic functionality, it also has a trade-off on mechanical stability. The observed structural deterioration is predominantly caused by thermal treatment.

Furthermore, the synthesized nanostructures exhibit distinctive characteristics, including the presence of macroscopic and microscopic fissures. Despite these imperfections, the structures maintain a high structural integrity. The advanced Al_2O_3 opal constructs, capped with a uniform TiO_2 film, introduce an interface characterized by a pronounced index contrast. Such a configuration is anticipated to substantially increase the efficiency of photonic elements by increasing reflectance owed to higher index mismatch, paving the way for significant advancements in the field of photonics.

CHAPTER 4: CONCLUSION AND FUTURE WORK

The future work in this field will involve a combination of ultra-precise deposition control using atomic layer deposition (ALD) and the high accuracy of Spectroscopic Ellipsometry. ALD allows for atomic-scale manipulation and layering of materials, enabling the creation of structures with ultra-precise control over thickness and composition. This precision, along with spectroscopic ellipsometry's ability to accurately determine refractive indices to a degree of e^{-4}, presents an effective approach in the predictive design and control of refractive index variations within 3D periodic nanolattices. These cylindrical lattices introduce anisotropy in light manipulation, yielding direction-dependent optical properties. This anisotropy in light behavior necessitates anisotropic index measurements. The research will also explore how refractive indices vary with different processing parameters, including alterations in sphere sizes for colloidal lithography and adjustments in resist heights.

Additionally, my PhD research will delve into the simulations of reflectance in multilayer nanolattices using Rigorous Coupled-Wave Analysis (RCWA) simulations and Finite-Difference Time-Domain (FDTD) analysis through ANSYS Lumerical. These advanced simulation techniques are crucial for understanding and designing nanolattices that demonstrate perfect reflectance at specific, tailored design wavelengths. The goal is to achieve a level of mastery in the fabrication of nanolattices, leveraging the ultra-precise control of refractive indices to an order of e^{-4}. This will lead to the production of multilayer nanolattices with spatially variable refractive indices and geometries, optimized to function as highly efficient photonic crystals at predetermined wavelengths.

The project also aims to push the boundaries of current knowledge in thermal properties of these nanolattices. We plan to employ advanced thermal characterization techniques to explore their potential use in thermal insulation, specifically for cryogenic liquid hydrogen storage containers. This aspect of the research is particularly significant given the growing interest in hydrogen as a clean energy source and the challenges associated with its storage. In summary, this research will not only contribute to the field of nanophotonics and materials science but also has potential implications for energy storage and management, thereby addressing some of the critical challenges in sustainable energy and advanced material engineering.

REFERENCES

1. J. Wang, H. L. Duan, Z. P. Huang, and B. L. Karihaloo, Proc. R. Soc. A 462, 2069 (2006). https://doi.org/10.1098/rspa.2005.1637

2. S. Wu, Z. Weng, X. Liu, K. W. K. Yeung, and P. K. Chu, Adv. Funct. Mater. 24, 5464 (2014). https://doi.org/10.1002/adfm.201400706

3. J. Bauer, L. R. Meza, T. A. Schaedler, R. Schwaiger, X. Zheng, and L. Valdevit, Adv. Mater. 29, 1701850 (2017). https://doi.org/10.1002/adma.201701850

4. X. Zheng et al, Science 344, 1373 (2014). https://doi.org/10.1126/science.1252291

5. N. G. Dou, R. A. Jagt, C. M. Portela, J. R. Greer, and A. J. Minnich, Nano Lett. 8, 4755 (2018). https://doi.org/10.1021/acs.nanolett.8b01191

6. G. P. Zhang, C. Z. Wang, and K. M. Ho, Phys. Lett. A 375, 1043 (2011). https://doi.org/10.1016/j.physleta.2010.12.082

7. L. Braginsky, V. Shklover, H. Hofmann, and P. Bowen, Phys. Rev. B 70, 134201 (2004). https://doi.org/10.1103/PhysRevB.70.134201

8. R. Anufriev, J. Maire, and M. Nomura, Phys. Rev. B 93, 045411 (2016). https://doi.org/10.1103/PhysRevB.93.045411

9. Y. Zhao, W. Wan, Y. Chen, R. Erni, C. A. Triana, J. Li, C. K. Mavrokefalos, Y. Zhou, and G. R. Patzke, Adv. Energy Mater. 10, 2002228 (2020). https://doi.org/10.1002/aenm.202002228

10. E. Yablonovitch, Phys. Rev. Lett. 58, 2059 (1987). https://doi.org/10.1103/PhysRevLett.58.2059

11. J. D. Joannopoulos, P. R. Villeneuve, and S. Fan, Nature 386, 143 (1997). https://doi.org/10.1038/386143a0

12. Y. Fink, J. N. Winn, S. Fan, C. Chen, J. Michel, J. D. Joannopoulos, and E. L. Thomas, Science 282, 1679 (1998). https://doi.org/10.1126/science.282.5394.1679

13. J. Q. Xi, J. K. Kim, and E. F. Schubert, Nano Lett. 5, 1385 (2005). https://doi.org/10.1021/nl050698k

14. J.-H. Min, X. A. Zhang, and C. H. Chang, Opt. Express 24, A276 (2016). https://doi.org/10.1364/OE.24.00A276

15. J. Q. Xi, J. K. Kim, E. F. Schubert, D. Ye, T. M. Lu, S. Y. Lin, and J. S. Juneja, Opt. Lett. 31, 601 (2006). https://doi.org/10.1364/OL.31.000601

16. N. Kawakami, Y. Fukumoto, T. Kinoshita, K. Suzuki, and K. I. Inoue, Jpn. J. Appl. Phys. 39, L182 (2000). https://doi.org/10.1143/JJAP.39.L182

17. M. Daimon and A. Masumura, Appl. Opt. 41, 5272 (2002). https://doi.org/10.1364/AO.41.005275

18. Vukusic, P. & Sambles, J. R. Photonic structures in biology. Nature 424, 852–855 (2003).

19. Chen, Y.-A., Naidu, S. V., Luo, Z. & Chang, C.-H. Enhancing optical transmission of multilayer composites using interfacial nanostructures. Journal of Applied Physics 126, 063101 (2019).

20. Park, K.-C. et al. Nanotextured Silica Surfaces with Robust Superhydrophobicity and Omnidirectional Broadband Supertransmissivity. ACS Nano 6, 3789–3799 (2012).

21. Luo, Z., Evans, B. A. & Chang, C.-H. Magnetically Actuated Dynamic Iridescence Inspired by the Neon Tetra. ACS Nano 13, 4657–4666 (2019).

22. Nosonovsky, M. & Bhushan, B. Roughness optimization for biomimetic superhydrophobic surfaces. Microsyst Technol 11, 535–549 (2005).

23. X. A. Zhang, A. Bagal, E. C. Dandley, J. Zhao, C. J. Oldham, B. I. Wu, G. N. Parsons, and C. H. Chang, Adv. Func. Mater. 25, 6644 (2015). https://doi.org/10.1002/adfm.201502854

24. J. Q. Xi, M. F. Schubert, J. K. Kim, E. F. Schubert, M. Chen, S. Y. Lin, W. Liu, and J. A. Smart, Nat. Photonics 1, 176 (2007). https://doi.org/10.1038/nphoton.2007.26

25. I. T. Chen, Z. Dai, D. T. Lee, Y. A. Chen, G. N. Parsons, and C. H. Chang, Adv. Mater. Interfaces 8, 2100690 (2021). https://doi.org/10.1002/admi.202100690

26. J. A. Liddle, G. M. Gallatin, ACS Nano 10, 2995 (2016). https://doi.org/10.1021/acsnano.5b03299

27. M. H. Yoo, Metall. Mater. Trans. A 12, 409 (1981). https://doi.org/10.1007/BF02648537

28. M. J. Madou, Fundamentals of Microfabrication: The Science of Miniaturization, 2nd ed. (CRC, Boca Raton, FL, 2002).

29. L. Wu, Y. Zhong, C. T. Chan, K. S. Wong, and G. P. Wang, Appl. Phys. Lett. 86, 241102 (2005). https://doi.org/10.1063/1.1947369

30. S. Jeon, J. U. Park, R. Cirelli, S. Yang, C. E. Heitzman, P. V. Braun, P. J. A. Kenis, and J. A. Rogers, Proc. Natl. Acad. Sci. U.S.A. 101, 12428 (2004). https://doi.org/10.1073/pnas.0403048101

31. J. K. Hyun, J. U. Park, E. Kim, L. J. Lauhon, and S. Jeon, Adv. Opt. Mater. 2, 1213 (2014). https://doi.org/10.1002/adom.201400348

32. C. H. Chang, L. Tian, W. R. Hesse, H. Gao, H. J. Choi, J. G. Kim, M. Siddiqui, and G. Barbastathis, Nano Lett. 11, 2533 (2011). https://doi.org/10.1021/nl2011824

33. A. Bagal et al, Sci. Rep. 7, 9145 (2017). https://doi.org/10.1038/s41598-017-09521-6

34. X. A. Zhang, I. T. Chen, and C. H. Chang, Nanotechnology 30, 352002 (2019). https://doi.org/10.1088/1361-6528/ab2282

35. M. D. Groner, F. H. Fabreguette, J. W. Elam, and S. M. George, Chem. Mater., 16, 4, 639–645 (2004). https://doi.org/10.1021/cm0304546

36. M. Leskelä and M. Ritala, Thin Solid Films 409, 138 (2002). https://doi.org/10.1016/S0040-6090(02)00117-7

37. T. A. Schaedler, A. J. Jacobsen, A. Torrents, A. E. Sorensen, J. Lian, J. R. Greer, L. Valdevit, and W. B. Carter, Science 334, 962 (2011).https://doi.org/10.1126/science.1211649

38. L. R. Meza, S. Das, and J. R. Greer, Science 345, 1322 (2014).https://doi.org/10.1126/science.1255908

39. L. C. Montemayor, L. R. Meza, and J. R. Greer, Adv. Eng. Mater. 16, 184 (2014). https://doi.org/10.1002/adem.201300254

40. L. R. Meza and J. R. Greer, J. Mater. Sci. 49, 2496 (2014). https://doi.org/10.1007/s10853-013-7945-x

41. V. Hahn, P. Kiefer, T. Frenzel, J. Qu, E. Blasco, C. B. Kowollik, and M. Wegener, Adv. Funct. Mater. 30, 1907795 (2020).https://doi.org/10.1002/adfm.201907795

42. H. W. P. Koops, R. Weiel, D. P. Kern, and T. H. Baum, J. Vac. Sci. Technol. B 6, 477 (1988).https://doi.org/10.1116/1.584045

43. A. Botman, J. J. L. Mulders, and C. W. Hagen, Nanotechnology 20, 372001 (2009). https://doi.org/10.1088/0957-4484/20/37/372001

44. C. V. Shank and R. V. Schmidt, Appl. Phys. Lett. 23, 154 (1973).https://doi.org/10.1063/1.1654841

45. J.-H. Jang, C. K. Ullal, M. Maldovan, T. Gorishnyy, S. Kooi, C. Koh, and E. L. Thomas, Adv. Funct. Mater. 17, 3027 (2007).https://doi.org/10.1002/adfm.200700140

46. J. Y. Cheng, C. A. Ross, H. I. Smith, and E. L. Thomas, Adv. Mater. 18, 2505 (2006).https://doi.org/10.1002/adma.200502651

47. C. A. Ross, K. K. Berggren, J. Y. Cheng, Y. S. Jung, and J.-B. Chang, Adv. Mater. 26, 4386 (2014).https://doi.org/10.1002/adma.201400386

48. J. Wen, Y. Zhang, and M. Xiao, Adv. Opt. Photonics 5, 1 (2013).https://doi.org/10.1364/AOP.5.000083

49. I.-T. Chen, F. R. Poblete, A. Bagal, and C.-H. Chang, Proc. Natl. Acad. Sci. U. S. A. 119, 38 (2022).https://doi.org/10.1073/pnas.2201589119

50. S. M. George, Chem. Rev. 110, 111 (2010). https://doi.org/10.1021/cr900056b

51. V. A. Premnath, I.-T. Chen, K.-C. Chien, and C.-H. Chang, J. Vac. Sci. Technol. B 40, 062803 (2022). https://doi.org/10.1116/6.0002112

52. A. Bagal, "Multifunctional periodic 3D thin-Shell nanostructures," Ph.D. thesis (North Carolina State University, 2016).

53. A. Rothen, Rev. Sci. Instrum. 16, 26 (1945). https://doi.org/10.1063/1.1770315

54. V. A. Markel, J. Opt. Soc. Am. A 33, 7 (2016). https://doi.org/10.1364/JOSAA.33.001244

55. P. Panthong, S. Srisuphaphon, A. Pattanaporkratana, S. Chiangga, and S. Deachapunya, Appl. Opt. 57, 1657 (2018). https://doi.org/10.1364/AO.57.001657

56. I. T. Chen, E. Schappell, X. Zhang, and C. H. Chang, Microsyst. Nanoeng. 6, 22 (2020). https://doi.org/10.1038/s41378-020-0133-7

57. H. Duan, J. K. W. Yang, and K. K. Berggren, Nano Micro Small 7, 2661 (2011). https://doi.org/10.1002/smll.201100892